

Comparison of Global H I and H α Line Profiles in MaNGA Galaxy Pairs with FAST

GAOXIANG JIN ^{1,2}, Y. SOPHIA DAI ², CHENG CHENG ², CONG KEVIN XU ², JIA-SHENG HUANG ^{2,3} AND LIHWAI LIN ⁴

¹Max Planck Institute for Astrophysics, Karl-Schwarzschild-Str. 1, D-85741, Garching, Germany

²Chinese Academy of Sciences South America Center for Astronomy (CASSACA), National Astronomical Observatories (NAOC), 20A Datun Road, Beijing 100012, China

³Center for Astrophysics | Harvard-Smithsonian, 60 Garden Street, Cambridge, MA 02138, USA

⁴Institute of Astronomy & Astrophysics, Academia Sinica, Taipei 10617, Taiwan

ABSTRACT

We present case studies comparing the global H I and H α emission line profiles of six galaxy pairs. The six pairs are selected to have different nuclear activities, with two hosting an active galactic nucleus, and in different merging stages—two of each from pre-merging, merging, and post-merger stages. We observe their global H I spectra with the Five-hundred-meter Aperture Spherical radio Telescope (FAST), achieving a noise level of ~ 0.5 mJy. Five out of the six pair systems have secure detections of H I emissions (signal-to-noise ratio > 10). The H I fraction and star formation efficiency of the six pairs do not deviate from isolated galaxies. For the H I line profiles, common unique asymmetry is observed, indicating disturbances on the atomic gas from the galaxy interaction. The global H α spectra of the merger systems are constructed from the optical integral field spectroscopic observations, by integrating the flux in corresponding line-of-sight velocity bins. The H α spectra tend to show multiple components in the pre-merger phase, and single component line profiles in the post-merger systems, while all H I spectra show single component line profiles regardless of merger stages. The H I and H α spectra show offsets in the central velocities, which appear to decrease from > 100 km s⁻¹ in the pre-merger pair to < 10 km s⁻¹ in the post-mergers. This trend is consistent with the scenario that, despite the significantly different distributions and kinematics of the atomic and ionized gases, the merging process may contribute to the mixing and eventually align various gas contents.

Keywords: Galaxy interactions (600) — H I line emission (690) — Interstellar line emission (844) — AGN host galaxies (2017)

1. INTRODUCTION

The interstellar and circumgalactic medium (ISM and CGM) play important roles in the ‘baryon cycle’ of the galaxy evolution. Observationally, galaxies consume gas through star formation and the accretion of supermassive black holes (SMBHs). The rapid consumption of gas indicates that galaxies have to obtain gas from the circumgalactic medium (CGM, e.g. Tumlinson et al. 2017). Also, the observed quenching of massive galaxies proves that there are mechanisms like ram pressure stripping (e.g. Gunn & Gott 1972) and AGN feedback (e.g. Fabian 2012), which can bring the gas away from the host galaxies and then stop the star formation. In simulations, galaxy-galaxy interactions and mergers are the common fast ways for gas to flow into galaxies. The gas inflow may enhance or trigger the star formation (e.g. Barnes & Hernquist 1992) and the fast accre-

tion of SMBHs (known as the active galactic nuclei, AGN) in merging systems (e.g. Hopkins et al. 2008).

The enhancements of star formation are widely found among interacting and merging star-forming galaxies (SFGs), based on their bluer color (e.g. Lin et al. 2007), stronger emission lines (e.g. Dai et al. 2021), and luminous infrared emission (e.g. Hwang et al. 2011). The strongest enhancements seem to occur in the central regions of SFGs (e.g. Pan et al. 2019). However, the merger impact on the star formation of individual galaxies is quite complex. Previous works revealed that the merger-triggered star formation enhancement is related to several different parameters, such as the merging stages (e.g. Pan et al. 2019), nuclear properties (Jin et al. 2021), pair distance (e.g. Patton et al. 2011), mass ratio (e.g. Ellison et al. 2008), morphology (Xu et al. 2010), and bulge masses (He et al. 2022). Jin et al. (2021) recently revealed that the galaxy-galaxy interaction can enhance the star formation in SFG pairs, but this effect is not significant in narrow-line selected AGN-host galaxies or quiescent galaxies. This difference may be directly related to the galaxy types, particularly their gas abundance, since the narrow-line AGNs and quiescent galaxies are known to be

more gas-deficient than SFGs (Saintonge et al. 2017; Ellison et al. 2019).

For nearby galaxies, hydrogen gas is a major contributor to ISM and CGM. The physical condition, spatial distribution, and kinematics of the hydrogen gas offer information and precious probes for studying the physical and chemical processes during galaxies' evolution. Based on the different temperatures and pressures, hydrogen in the ISM and CGM exists mainly in three phases: the atomic, ionized, and molecular gas. The neutral atomic gas (H I) and ionized gas can be directly measured through the fine structure emission line at 21 cm and the recombination lines at optical wavelengths, respectively.

H I, as the most abundant and extended gas content in galaxies, is the ideal indicator to study the kinematics of galaxy pair systems. Simulations showed that the tidal forces during galaxy interaction can trigger gas flows into the galaxy center (e.g. Barnes & Hernquist 1996), while the resulted star formation or AGN activity would quickly consume or blow out the gas. Relevant and detailed observational evidence is still limited. Marginal global H I depletion ($\sim 15\%$) is only found in tens of nearby major mergers (Yu et al. 2022b), while Ellison et al. (2018) found a 0.3-0.6 dex enhancement of the H I fraction. To investigate the behavior of atomic gas during galaxy mergers, more kinematic information is needed from H I observations. Interferometry studies on nearby interacting mergers found discrepancies between the tidal tails of H I gas and stars (e.g. Hibbard & van Gorkom 1996; Hibbard et al. 2000; Iono et al. 2005). But mapping the mass and velocity distribution of H I in galaxies is time-consuming and requires radio interferometry arrays, making it expensive to build statistical galaxy merger samples with high resolution H I maps. An alternative approach is to estimate the asymmetry from the shape of the global H I line profile through unresolved single-dish observations. For instance, Bok et al. (2019) found that galaxy pairs tend to have more asymmetric global H I line profiles. Watts et al. (2021) and Zuo et al. (2022) suggested that although pair and merger systems tend to have unique single-peaked line profiles, there is no significant difference in the quantitative asymmetry distributions. A recent case study also shows that the H I content in a galaxy group can extend to hundreds of kpcs from the group center (Xu et al. 2022). Lin et al. (2023) also found H I stripping in interacting galaxy systems. These complex H I structures and kinematics in groups and pairs can be the reason of the observed global line asymmetry.

Compared to H I, ionized gas is a more direct tracer of star formation, since the hydrogen is mostly excited by the high energy photons from young stars. These star-forming regions, also known as the H II regions, are the main contributors to the recombination lines in normal galaxies (Osterbrock & Ferland 2006). The global line profiles of strong recombination lines, such as $H\alpha$, represent the global kinematics of the star formation component. Conventionally, the optical $H\alpha$ spectra of nearby galaxies are typically observed with narrow slit prisms or thin fibers, thus either along a certain direction or limited to the central regions of a galaxy. To

obtain the global line profile of $H\alpha$, optical spectra coverage is needed for the whole galaxy is needed. Integral field unit (IFU) offers the opportunity to build up the optical spectra of a galaxy.

Andersen et al. (2006) presented a pioneer work of comparing the global H I and $H\alpha$ line profiles of isolated face-on spirals. The global $H\alpha$ line profiles are built and tested from the narrow band $H\alpha$ imaging and the IFU. They found that most of the galaxies show agreement between the global H I and $H\alpha$ line width, but the line shapes are significantly different, indicating possibly different locations or dynamics. Andersen & Bershad (2009) and Watts et al. (2023) confirmed this conclusion in updated samples, and further investigated the origin of the asymmetry in both the global H I and $H\alpha$ lines. They suggested that the $H\alpha$ flux distribution typically dominates the asymmetry of the global $H\alpha$ spectra, and most global H I asymmetries trace disturbances in the outer regions of the host galaxies.

However, such studies are so far limited only to isolated, well-defined face-on galaxies. For galaxy mergers, the comparison between the atomic and ionized gas offers unique insight about the global gas kinematics and distributions during the merger event. It is suspected that the discrepancies between the asymmetry of $H\alpha$ and H I result from strong perturbations in the galaxy scale, such as galaxy mergers (Watts et al. 2023).

A sample of galaxy pairs and mergers with both IFU and H I observations can be useful to examine whether galaxy interactions would induce different line profiles between $H\alpha$ and H I emissions. One of the largest IFU surveys, Mapping the Nearby Galaxies at APO (MaNGA, Bundy et al. 2015), has observed ~ 10000 nearby galaxies. MaNGA observes the target galaxies out to 1.5 r -band effective radii (R_e), meaning that the fiber bundles can cover most of the stellar and ionized gas component of the galaxies, or in pairs. There is also a large sample of ~ 1000 merging galaxies observed by MaNGA (Pan et al. 2019; Jin et al. 2021). We take these advantages and select a pair sample to compare the global H I and $H\alpha$ line profiles.

H I line profile analysis needs high signal-to-noise ratio as well as enough velocity resolution. For MaNGA galaxies at $z < 0.05$, H I-MaNGA (Masters et al. 2019) is the ongoing H I follow-up survey. Its data include the proposed new observations using the Robert C. Byrd Green Bank Telescope (GBT), and the archive results from the Arcibo Legacy Fast ALFA survey (ALFALFA, Giovanelli et al. 2005), with the spectra root-mean-square (rms) of ~ 1.5 mJy and ~ 3.5 mJy, respectively (velocity resolution ~ 10 km s $^{-1}$). The GBT observation can only reach the signal-to-noise ratio (S/N) of 3 on a $z = 0.02$ galaxy with $M_{\text{HI}} = 9.4 M_{\odot}$. In this paper, we use the Five-hundred-meter Aperture Spherical radio Telescope (FAST, Nan 2006) to observe our six pair systems and to get deeper observations (rms < 0.5 mJy, $\Delta v = 10$ km s $^{-1}$, $\sim 3 - 10\times$ deeper than H I-MaNGA), which is powerful and necessary to analyze the line profile shapes of the H I spectra. Additionally, the large beam size (~ 2.9 arcmin) of FAST (Jiang et al. 2020) can offer us the

global H I line profiles tracing the atomic gas environment of the whole merger systems. Along with the global H α line profiles constructed from MaNGA, here we present case studies to compare the kinematics of the atomic gas and ionized gas in nearby merging systems.

The paper is constructed as follows: In Section 2 we introduce the target selection and the data product. In Section 3 and Appendix A we present our FAST data reduction procedure in detail. Section 4 is the scientific analysis, in which we compare the FAST H I spectra with the integrated MaNGA H α spectra for each galaxy pair system. We measure the H I fraction and the atomic gas SFE and compare them with other H I surveys in Section 5.

Throughout this paper, the velocities are calculated by $c \times z$, where c is the speed of light and $1+z = \nu_0/\nu = \lambda/\lambda_0$, and are then converted to the local standard of rest (LSR) frame. We adopt a cosmology with $H_0 = 70 \text{ km s}^{-1} \text{ Mpc}^{-1}$, $\Omega_m = 0.3$, and $\Omega_\Lambda = 0.7$. All stellar masses and star formation rates are based on the Kroupa initial mass function (Kroupa 2001).

2. TARGET SELECTION AND SAMPLE PROPERTIES

2.1. MaNGA

MaNGA is one of the main surveys of the fourth generation of the Sloan Digital Sky Survey (SDSS-IV, Bundy et al. 2015), which has obtained the IFU spectra for over 10 000 nearby galaxies. The field of views (FOVs) of the MaNGA science IFUs vary in diameter from 12'' to 32'', which cover most of the stellar component of our targets. The 2'' fibers have a spatial resolution of $\sim 1 \text{ kpc}$ at $z=0.03$. The spectral resolution ($\lambda/\Delta\lambda$) is about ~ 2000 at the H α wavelength (Smee et al. 2013). Our analysis in this paper is based on the latest public data release, MaNGA Product Lanuch 11 (the same as SDSS DR17, Abdurro'uf et al. 2022).

Our parent sample is the MaNGA galaxy pair sample used in Jin et al. (2021). This parent sample includes 994 IFU-covered galaxies in pairs. Morphologically, the pair systems are visually classified into merger cases from pre-merging (isolated) to the final coalescence (post-merger). The sample is classified into narrow-line AGNs, composite galaxies, star-forming galaxies, and quiescent galaxies based on the emission line ratio diagnostics. Here we refer the readers to Jin et al. (2021) for more details about the pair selection, merger stage definition, and the AGN classification.

We use the redshifts and stellar masses in MaNGA's parent sample catalog, the NASA-Sloan-Atlas¹. These redshifts are derived from the SDSS spectra, which are observed by single fibers targeting at the photometric center of the galaxies. The stellar masses are calculated from the multiwavelength spectral energy distribution (SED) fitting (Blanton & Roweis 2007). The photometries used for the fitting include UV bands from GALEX (The Galaxy Evolution Explorer, Martin et al. 2005) and optical bands from SDSS. The results

based on elliptical Petrosian aperture photometries are chosen to reduce the uncertainty due to irregular morphologies of galaxy pairs. The global star formation rates are calculated by the attenuation-corrected H α luminosities, following Kennicutt & Evans (2012):

$$\log\left(\frac{\text{SFR}}{M_\odot \text{ yr}^{-1}}\right) = \log\left(\frac{L_{\text{H}\alpha}}{\text{erg s}^{-1}}\right) - 41.27. \quad (1)$$

The $L_{\text{H}\alpha}$ is based on the integrated spectra in MaNGA's FOV and corrected for attenuation by assuming an intrinsic H α /H β =2.86 (Case B recombination, Osterbrock & Ferland 2006) and the reddening curve from Cardelli et al. (1989): $L_{\text{H}\alpha} = L_{\text{H}\alpha, \text{obs}} \times [(\text{H}\alpha/\text{H}\beta)_{\text{obs}}/2.86]^{2.36}$. We use the results from MaNGA Data Analysis Pipeline (DAP, Belfiore et al. 2019; Westfall et al. 2019) for the H α flux and velocity measurements.

2.2. Target selection

For the FAST observations, we selected six pair systems to represent different merging stages and pair types. We restrict the pairs to have spectroscopic redshifts of $z < 0.03$, in order to reach high S/N and avoid radio frequency interference (RFI) at lower frequencies (Jiang et al. 2020). Within 3 arcmins, there are no galaxies at similar redshift (i.e., $\Delta v < 2000 \text{ km s}^{-1}$), which ensures that the pairs are physically isolated in the FAST central beam and the H I observations are not contaminated by nearby sources. To cover different galaxy pairs along the merger sequence and compare the differences, we select two pairs in each merger stage: pre-merging stage (weak or no distortion), merging stage (strong distortion), and post-merger stage (coalescenced mergers). There are two AGN host galaxies in the merging and post-merger stages, respectively. This selection is made to enable the comparison of the H I line profiles for AGN pairs and non-AGN pairs.

The MaNGA Plate-IFU numbers, sky coordinates, redshifts, AGN classification results, global stellar masses and SFRs, and merger stages of the six pair systems are summarized in Table 1. Fig. 1 shows the global stellar masses and SFRs of the member galaxies in our pairs or the pair systems if not separable. The two AGNs, as well as the SFGs in the pairs, all lie along the star formation main sequence (SFMS) from Renzini & Peng (2015).

3. FAST OBSERVATION AND DATA REDUCTION

3.1. Observational settings

The FAST observations were carried out in the latter half of 2021 during the shared-risk period (proposal ID: PT2020-0160). We used the L-band and the central beam (M01) of the FAST 19-beam receiver to observe the H I emission lines. The systematic performance, such as aperture efficiency, pointing accuracy, and system temperature, has been tested and discussed in Jiang et al. (2020). The frequency coverage of FAST L-band is from 1.05 GHz to 1.45 GHz,

¹ NSA; M. Blanton; <http://www.nsatlas.org/>

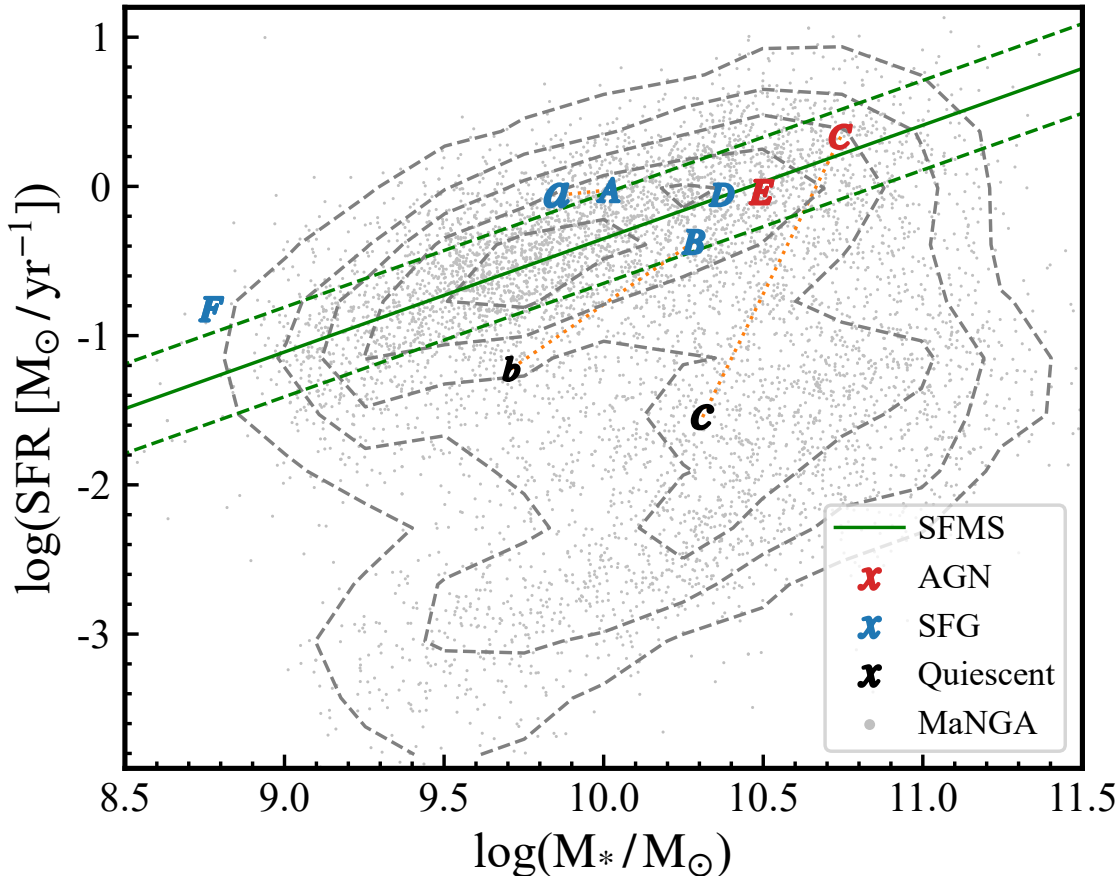


Figure 1. The stellar masses and SFRs of the galaxies in our six pair systems, overlaid on the overall SFR- M_* distribution (grey dots and contour) of all MaNGA galaxies at $z < 0.05$. The star formation main sequence (SFMS) as well as the typical scatter (± 0.3 dex) are taken from [Renzini & Peng \(2015\)](#) and shown in green lines. If separable, the stellar mass and SFR of the two member galaxies in a pair are plotted individually and connected by the orange dotted lines. Galaxies in the same pair share the same symbols, and are color-coded by their BPT types.

with a channel resolution of 7.63 kHz (velocity resolution ~ 1.6 km/s at $z \sim 0.02$). The average half-power beamwidth of the central beam is ~ 2.9 arcmin. Since the beamsize is ~ 80 kpc in physical size at the targeted redshift, much larger than the sizes of our pair systems (< 1 arcmin), the H I content outside the central beam is not considered.

We adopt the ON-OFF observation mode, switching every five minutes. The ON point of beam M01 is set at the galaxy pair, while the OFF pointings are set at background skies tens of arcmins away, chosen to have no galaxies at similar redshift. Thus, the OFF pointings can serve as the approximate baselines at the target frequencies. The high-power calibration noise is injected during the first 20 seconds of each ON/OFF observation.

3.2. Data reduction

At the time of observation, FAST was still improving its performance especially the RFI issues and did not have a finalized data reduction pipeline. We adopted the instrument parameters provided by [Cheng et al. \(2020\)](#), and built our

own pipeline for our observation settings to reduce the data. Our detailed 4-step data reduction procedure can be found in [Appendix A](#), and is briefly summarized below. We first manually identify and remove the time-domain RFIs, and then perform the temperature calibrations for each exposure, the standing waves baseline removal is carried out for the ON minus OFF spectra, before converting to flux unit, and smoothing the stacked spectra to measure the H I emissions. The observation settings and spectral properties are listed in [Table 2](#). The integration time (t_{Intn}) is the ‘real’ ON duration after removing the time affected by RFIs.

After the stacked H I spectra have been obtained, we calculate the H I mass using the relation as firstly derived by [Roberts \(1975\)](#). Assuming that the H I emission is optically thin and unresolved by the single-dish telescope beam, the H I mass can be calculated as

$$\frac{M_{\text{HI}}}{M_{\odot}} = \frac{2.36 \times 10^5}{(1+z)^2} \left(\frac{D}{\text{Mpc}}\right)^2 \int S(v)dv, \quad (2)$$

Table 1. Global properties of the 6 pair systems observed by FAST

| Pair ID | Plate-IFU | R.A. | Decl. | Optical z | BPT Class | M_* | SFR | Merger Case |
|---------|------------|----------|---------|-------------|-----------|-----------------|---------------------------|-------------|
| | | deg | deg | | | $\log(M_\odot)$ | $M_\odot \text{ yr}^{-1}$ | |
| (1) | (2) | (3) | (4) | (5) | (6) | (7) | (8) | (9) |
| A | 9194-12701 | 46.5605 | -0.3444 | 0.0287 | SFG | 10.01 | 0.94 | Pre-merging |
| a | 9194-12701 | 46.5574 | -0.3416 | 0.0294 | SFG | 9.85 | 0.87 | |
| B | 8254-12701 | 161.1697 | 44.0661 | 0.0258 | SFG | 10.28 | 0.36 | Pre-merging |
| b | N/A | 161.1447 | 44.0413 | 0.0251 | Quiescent | 9.71 | 0.05 | |
| C | 8978-12705 | 249.5586 | 41.9388 | 0.0286 | AGN | 10.74 | 2.15 | Merging |
| c | 8601-1902 | 249.5576 | 41.9311 | 0.0280 | Quiescent | 10.37 | 0.02 | |
| D | 8241-12705 | 127.6320 | 18.2061 | 0.0269 | SFG | 10.37 | 0.88 | Merging |
| E | 9507-12704 | 129.6001 | 25.7545 | 0.0182 | AGN | 10.49 | 0.92 | Post-merger |
| F | 8725-9101 | 126.8250 | 46.0326 | 0.0073 | SFG | 8.77 | 0.15 | Post-merger |

NOTE—(1): Galaxies in the same pair are represented in the same letter but in different cases, with the capital letter denoting the more massive member galaxy. (2): The MaNGA Plate-IFU number of the galaxies. (3)&(4): The sky coordinates of the galaxies. (5): Redshifts derived from SDSS optical spectra. (6): BPT classification for the galaxy centers using MaNGA spectra. (7)&(8): Global stellar masses and SFRs of the galaxies (or the whole pair systems if the members are not separable). (9): The merger stages.

where $S(v)$ is the line flux density² in Jy, and D is the luminosity distance of the galaxy. For non-detections we assume a line-width of 300 km s^{-1} and integrate the rms as the upper limit of the H I mass.

The measured and calculated H I properties are listed in Table 3. The signal-to-noise ratio (SNR) is calculated by the ratio of the peak flux (after Hanning-smooth) and the rms. We also compare the sensitivity of FAST with other telescopes in Appendix B. The central H I velocities (v_{center}) are calculated as the mean value of the right and left wing velocities, which are defined as the velocities at the 50% of the peak flux for both sides of the emission line. The wing velocity widths (W_{P50}) are defined as the width of the HI line measured at 50% of the peak between both sides, the same as in the H I-MaNGA survey (Masters et al. 2019). Values of the 50% cumulative flux velocities ($v_{c50, \text{H}\alpha}$, $v_{c50, \text{HI}}$), as shown in Figure 3, Figure 5, and Figure 6, while Δv_{c50} is the difference between $v_{c50, \text{HI}}$ and $v_{c50, \text{H}\alpha}$, and will be discussed in Section 4.7.

4. LINE PROFILE COMPARISON OF H I AND H α

² Here Jy and Jy beam^{-1} are the same for the flux density since all the sources are unresolved.

In this section, we directly compare the H α emission line profiles from MaNGA IFU data with the FAST H I line profiles. Below we perform a case-by-case study of the ionized gas and atomic gas properties in our galaxy mergers.

The H I line profiles of six pair systems are shown in Fig. 2, where the velocity resolution is smoothed to $\sim 3.3 \text{ km s}^{-1}$. Compared to the archival H I-MaNGA survey observations (green dashed lines), our results show clear improvements in both SNR and spectral resolution. For the H α flux density-velocity line profiles, we use all valid spaxels within the whole MaNGA FOV and sum the H α fluxes in velocity bins of 20 km s^{-1} . The velocity of each spaxel is calculated by $c \times z_{\text{H}\alpha}$ and then converted to the LSR frame. We chose the velocity bin of 20 km s^{-1} because Law et al. (2021) concluded that the MaNGA spectra can provide reliable measurements of astrophysical velocity dispersions $\sigma_{\text{H}\alpha} \sim 20 \text{ km s}^{-1}$.

The long transition time ($\sim 10^7$ years) of the H I line means that the H I line profile represents the Doppler motion of the atomic gas (e.g. Pritchard & Loeb 2012), while the H α line is more likely to be affected by the other broadening mechanisms, for example, the normal turbulent motions of ionized gas can increase the $\sigma_{\text{H}\alpha}$ to $\sim 25 \text{ km s}^{-1}$ (e.g. Andersen et al. 2006), while some violent processes like shock and winds can increase the $\sigma_{\text{H}\alpha}$ to $\gtrsim 100 \text{ km s}^{-1}$ (e.g. Davies et al. 2017). So, the H α fluxes and velocities used for global line profiles are calculated from the Gaussian fit on MaNGA spectra without the velocity dispersion ($\sigma_{\text{H}\alpha}$) information. This way the H α line profiles can approximately represent the global rotation of the ionized gas and are less

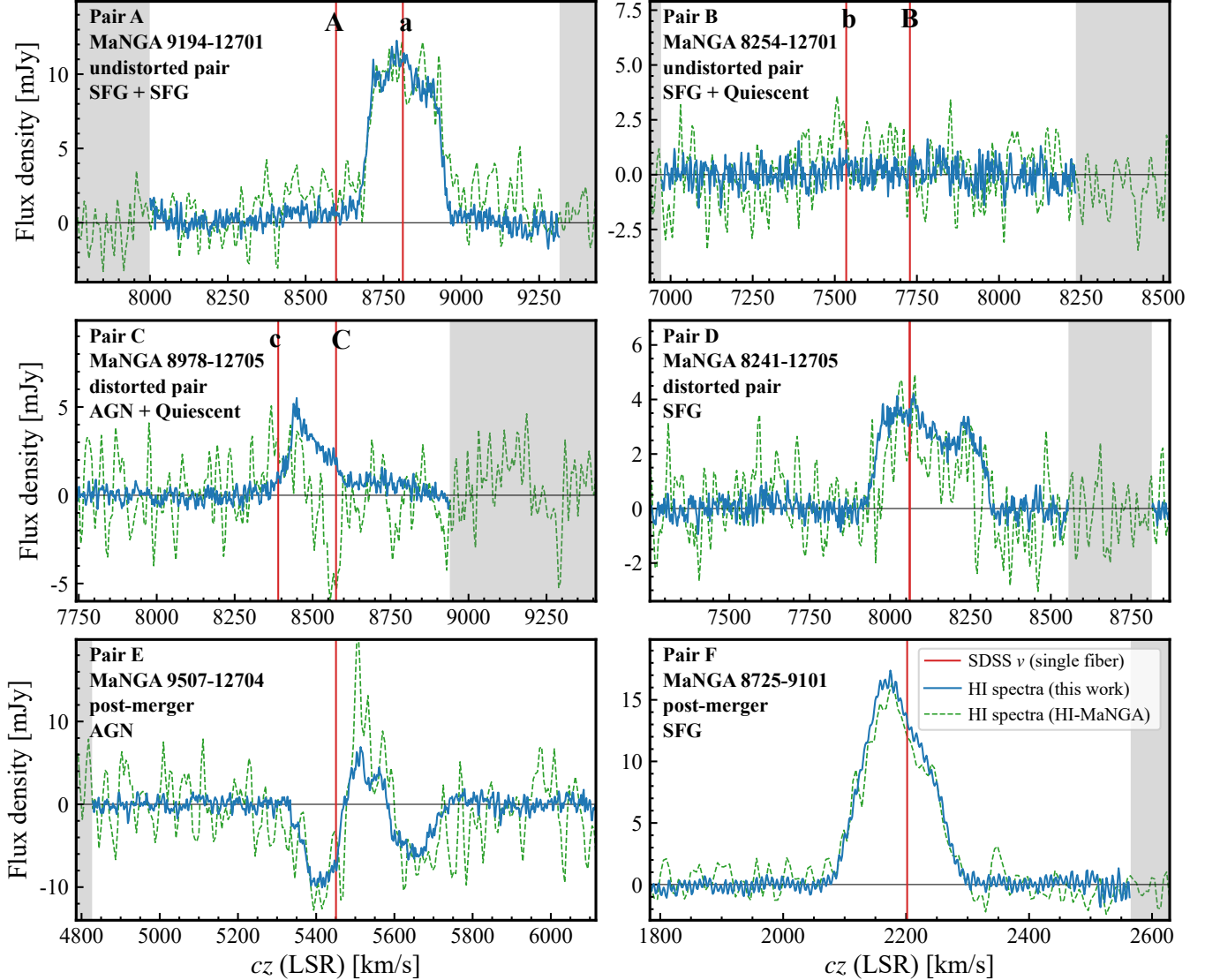


Figure 2. The H I spectra of our six pair systems. In blue are our FAST results with a velocity resolution of about 3.3 km s^{-1} . Red solid lines mark the optical velocities from SDSS single fiber spectra of the pair member(s), measured at the optical photometric center(s). The redshifts of each member in Pair A, B, C are also labeled by their pair ID. The frequencies affected by severe frequency-domain RFIs are masked and shown as gray shaded regions same as the yellow regions in Fig. A1. For comparison, the archival spectra from the H I-MaNGA survey (Masters et al. 2019) are plotted in green dashed lines. The velocity resolution is $\sim 10 \text{ km s}^{-1}$ with a typical on-target integration time of $\sim 1000 \text{ s}$. FAST observations show significant improvement in both the spectral resolution and the signal-to-noise ratio.

affected by broadening from winds and shocks, thus can be compared to the single-dish H I line profiles directly.

For comparison, we then normalize the H I and the $H\alpha$ global line profiles and plot them in the same LSR frame, for a direct comparison of the atomic gas and ionized gas flux distribution along the line-of-sight velocities. Here the $H\alpha$ flux is not corrected for attenuation, since the $H\beta$ line has low S/N in galaxy outskirts, making the attenuation correction unreliable. In addition, we check the attenuation (e.g., A_V) calculated from the Balmer decrement, and find that the differences between the A_V in the central $2.5''$ and the A_V in

R_e are around 0.5, thus the attenuation correction should not affect our global line shape.

Fig. 3, 5, and 6 show the comparison of $H\alpha$ and H I line profiles of the pre-merging pairs, merging pairs, and post-mergers, respectively. In these figures, the SDSS color images are shown in the right with the magenta hexagons and white circles representing the MaNGA FOV and FAST beam, respectively. Pair members that are distinguishable are labeled in red text if available. In the main panels, gray lines H I spectra and green dashed lines are integrated $H\alpha$ spectra. The $H\alpha$ velocity maps are plotted near the spectra, with $H\alpha$ flux maps shown in black dashed contours. The colors are

Table 2. Observational settings

| Pair ID | ON R.A. | ON Decl. | OFF R.A. | OFF Decl. | t_{Int} |
|---------|-------------|-------------|-------------|-------------|------------------|
| - | - | - | - | - | s |
| (1) | (2) | (3) | (4) | (5) | (6) |
| Pair A | 03:06:14.39 | -00:20:37.9 | 03:04:33.28 | -00:31:06.2 | 1482.9 |
| Pair B | 10:44:40.76 | +44:03:59.5 | 10:43:41.05 | +44:04:31.0 | 599.4 |
| Pair C | 16:38:14.44 | +41:56:33.2 | 16:41:28.69 | +42:00:00.6 | 2018.2 |
| Pair D | 08:30:31.53 | +18:12:16.1 | 08:29:38.14 | +18:24:29.9 | 2377.5 |
| Pair E | 08:38:24.12 | +25:45:15.0 | 08:37:36.08 | +26:07:56.5 | 299.0 |
| Pair F | 08:27:18.32 | +46:02:09.8 | 08:27:18.04 | +46:05:01.1 | 2400.0 |

Table 3. Observational results

| Pair ID | f_{peak} | rms | SNR | $\log(M_{\text{HI}})$ | v_{center} | W_{P50} | $v_{\text{c50,H}\alpha}$ | $v_{\text{c50,HI}}$ | Δv_{c50} |
|---------|-------------------|------|------|-----------------------|---------------------|--------------------|--------------------------|---------------------|-------------------------|
| - | mJy | mJy | - | $\log(M_{\odot})$ | km s^{-1} | km s^{-1} | km s^{-1} | km s^{-1} | km s^{-1} |
| (1) | (2) | (3) | (4) | (5) | (6) | (7) | (8) | (9) | (10) |
| Pair A | 12.26 | 0.45 | 24.6 | 9.96 | 8816 | 164 | 8666 | 8803 | 138 |
| Pair B | 1.45 | 0.50 | - | <8.26 | - | - | - | - | - |
| Pair C | 5.51 | 0.34 | 16.2 | 9.42 | 8518 | 142 | 8465 | 8503 | 38 |
| Pair D | 4.21 | 0.29 | 14.5 | 9.50 | 8136 | 209 | 8086 | 8100 | 14 |
| Pair E | 6.83 | 0.66 | 10.4 | - | - | - | - | - | - |
| Pair F | 17.38 | 0.46 | 37.4 | 8.40 | 2195 | 110 | 2175 | 2181 | 6 |

coded by the velocities, while the color bars are matched to the velocity axis, as an approximate link between the fluxes and the locations in the maps. The upper panels are the cumulative fluxes of H α and H I. The steeper slope indicates that the fluxes are more concentrative in line-of-sight velocities. The difference of the two 50% flux velocities represents the line-of-sight offset of the ionized and atomic gas.

4.1. Pair A (Fig. 3 upper panel)

The system includes two SFGs with small projected separation (8.7 kpc) but a larger velocity offset (214.5 km s^{-1}). There is no significant interaction feature, and the two galaxies show regular morphology and velocity maps, indicating they are likely in the pre-merger stage.

The MaNGA IFU covered most optical fluxes from both galaxies, and the H α line profile shows two galaxy components, one rotating disk with the double horn structure, and one complex profile with possible differential structures. The rotating disk component is more blueshifted and matched to the brighter galaxy in the lower right. The fainter, bluer galaxy in upper right shows the complex line profile. These

two H α components are also visually distinct in the velocity map, as well as the optical image, stellar velocity map, and H α velocity dispersion map (Fig. 4), which indicates that these two galaxies are kinematically distinct in the line-of-sight direction. This also confirms that they are in the pre-merging phase.

The H I line profile, however, only shows one component, which only matches the velocities of the fainter galaxy. At the velocity of the brighter galaxy, there are marginal signals weaker than 3σ . The difference in the line profiles indicates that the H I content of the pair may be associated with the fainter galaxy. It is not likely that the atomic gas has already mixed together in the pre-merging stage, because both the H I spectra and the optical morphology do not show any signs of asymmetry or disturbance.

4.2. Pair B (Fig. 3 lower panel)

This system includes an SFG and a quiescent galaxy with large projected separation (57.2 kpc). This is also a pre-merging pair system with no significant interaction features.

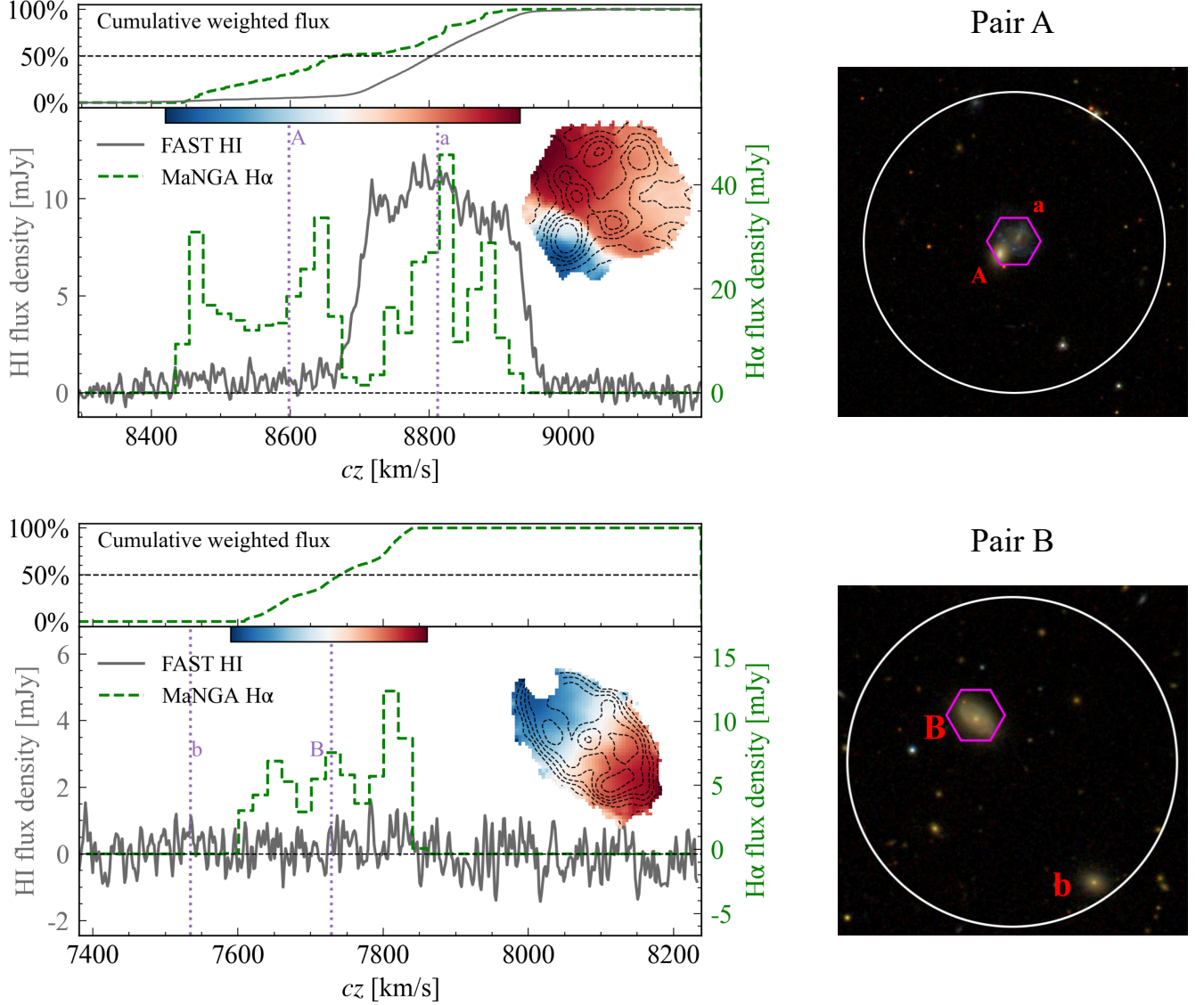


Figure 3. The comparison of global H α -H I spectra for pre-merging pairs A and B. Pair B is not detected in H I. The right panel shows the SDSS-*gri* color image, in which the magenta hexagon represents the MaNGA FOV and the white circle represents the FAST central beam location. The IDs of pair members are labeled near the galaxy positions. In the left panels, the gray lines and the green dashed lines are the cumulated H I and H α spectra, respectively. The SDSS redshifts are labeled in purple dashed lines, representing the optical velocities at the nuclear positions. The H α velocity maps from MaNGA are plotted in the panel, color coded by the line-of-sight velocities, with color bars and corresponding velocity ranges shown at the top of each spectra panel, along the velocity axis. Black dashed contours in the velocity maps are the H α flux maps. We also plot the cumulative spectra in the upper panels to distinguish the shapes between the two spectra. Their interceptions at the 50% flux can be used to represent the line-of-sight velocity offsets for H α and H I.

MaNGA covers the SFG and shows global star formation activity.

Although deeper than previous surveys such as H I-MaNGA, we still detect no significant H I signal. The $3\sigma N_{\text{HI}}$ limit is $2.8 \times 10^{18} \text{ cm}^{-2}$. We conclude that this is a relatively H I-poor system including one SFG and one quiescent galaxy. We note that even though the system is not detected for H I, the lower limit of the current atomic star

formation efficiency (SFE) is still within the intrinsic scatter of the general SFE distribution (see also Fig. 8).

4.3. Pair C (Fig. 5 upper panel)

The system includes a narrow-line AGN with distorted morphology and a quiescent galaxy, covered by two MaNGA IFUs. The clearly distorted morphology indicates that they are in the process of merging.

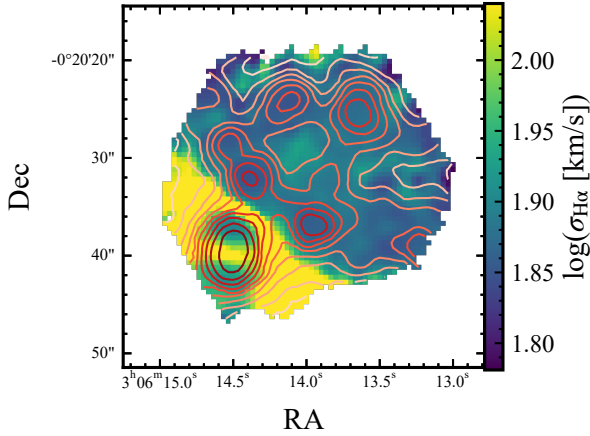


Figure 4. The $H\alpha$ velocity dispersion map of Pair A. The red contours are the $H\alpha$ flux density map. Despite the velocity differences, the two galaxies show clear different dispersions as well, indicating that the two members in the pair are kinematically distinct.

The $H\alpha$ flux concentrates near 8350 km s^{-1} , which is associated with a blueshifted star-forming region to the west of the central AGN. The total velocity coverage of $H\alpha$, as indicated by the color bar in Fig. 5, is about 500 km s^{-1} . The H I line profile is asymmetric, extending over a range of $> 400 \text{ km s}^{-1}$, with a long tail towards the red side of higher velocities. The highest peak of H I is $\sim 100 \text{ km s}^{-1}$ offset from the $H\alpha$ peak, while there is a second peak of H I at $\sim 8550 \text{ km s}^{-1}$, which coincides with the central $H\alpha$ peak at the same velocity, corresponding to the nuclear region of the AGN. We note that the $H\alpha$ from the southern galaxy (orange dotted line, amplified by 5 times, Fig. 5) is weaker compared to the northern AGN. The extended feature of the H I line profile also matches well with the $H\alpha$ fluxes at around $8600\text{--}8800 \text{ km s}^{-1}$. The seemingly aligned velocity profile longwards of 8500 km s^{-1} may indicate some intrinsic kinematic connection between the $H\alpha$ and H I components.

The observational star formation law (e.g. Kennicutt & Evans 2012) is well known to be a molecular rather than an atomic phenomenon (e.g. Bigiel et al. 2008), which disfavors the correlation between $H\alpha$ and H I in sub-galactic scales. But during galaxy mergers, the large-scale disturbance can have significant impact on the kinematics of all phases of gas, for instance, redistributing the galaxy in the system towards similar kinematics, which may eventually result in the line-of-sight velocity correlation between $H\alpha$ and H I. To confirm these implications, higher resolution radio interferometry observations are needed to confirm this hypothesis.

4.4. Pair D (Fig. 5 lower panel)

The system contains SFGs bridged together with clear tidal features. The morphological connection of the two pair members confirms that they are in the process of merging, probably already after the first encounter.

The wide H I emission, with a width of $\sim 400 \text{ km s}^{-1}$, fully covers and almost doubles the $H\alpha$ line width (~ 200

km s^{-1}). We note that the MaNGA IFU does not fully cover the pair system. The complete $H\alpha$ line width may be wider than observed if the southern tail extends to high velocity. Based on the $H\alpha$ velocity profile, the system is encountering volatile kinematics, with the two pair members and the tidal tails showing at several redshift/blueshift components. Similar to Pair C, this value is at the high end of the reported H I velocity width distributions in nearby galaxies (e.g. Zwaan et al. 2010; Yu et al. 2022a). Such high velocity width indicates that either the merging activity strongly disturbed the atomic gas to spread in a wider velocity space, or the H I spectra consists of several gas components of overlapping velocities, or a combination of both.

4.5. Pair E (Fig. 6 upper panel)

This is a clear post-merger system with two long, luminous tidal tails. It is classified as a narrow line AGN. MaNGA covers the central region, including the merger center and a luminous, blue star-forming region.

The $H\alpha$ components with the highest velocity component are close to the galaxy nucleus, where $\sigma_{H\alpha}$ also reaches $\sim 300 \text{ km s}^{-1}$ (σ_* is only $\sim 180 \text{ km s}^{-1}$), indicating a nucleus-driven line broadening. We also note that the long tails are not covered by MaNGA, the inclusion of the two tails may further widen the $H\alpha$ line profile. The H I spectra show two strong, broad absorption features. Given the broad line width of the absorption features in the H I line profile ($\sim 400 \text{ km s}^{-1}$), the absorption is possibly associated with the atomic gas related to the AGN and/or merger activities.

Follow-up high-resolution imaging and molecular gas observations are needed to identify the location and origin of the absorption feature. We note that this H I line profile shape, a central emission component with two strong absorption features at both wings, is rare and unique from most well-defined H I absorption galaxies (e.g. Geréb et al. 2015). The data reduction procedures are shown in Fig. A1 (c) and (d), and these features are not from the baseline fitting. The emission and absorption features in the spectrum from FAST observation are consistent with those of the ALFALFA archival observations, and the FAST spectrum shows a higher signal-to-noise ratio. We will discuss this object in more detail in an upcoming paper (Dai et al., in preparation).

4.6. Pair F (Fig. 6 lower panel)

This is a low-mass post-merger system with two separable nuclei in the optical image, covered in one MaNGA IFU. The two nuclei are both classified as SFGs by the emission line diagnostics.

We can clearly see two $H\alpha$ components from each galaxy in the flux map (top right corner, contours). The northern nucleus is slightly blueshifted while the southern nucleus is redshifted from the SDSS reported redshift. The $H\alpha$ flux map suggests two ionized gas cores around the optical center, and they are not yet fully merged. Thus, although the double-peaked shape of the global $H\alpha$ spectra could be created by a global rotation, it could also be explained by a mixture of two

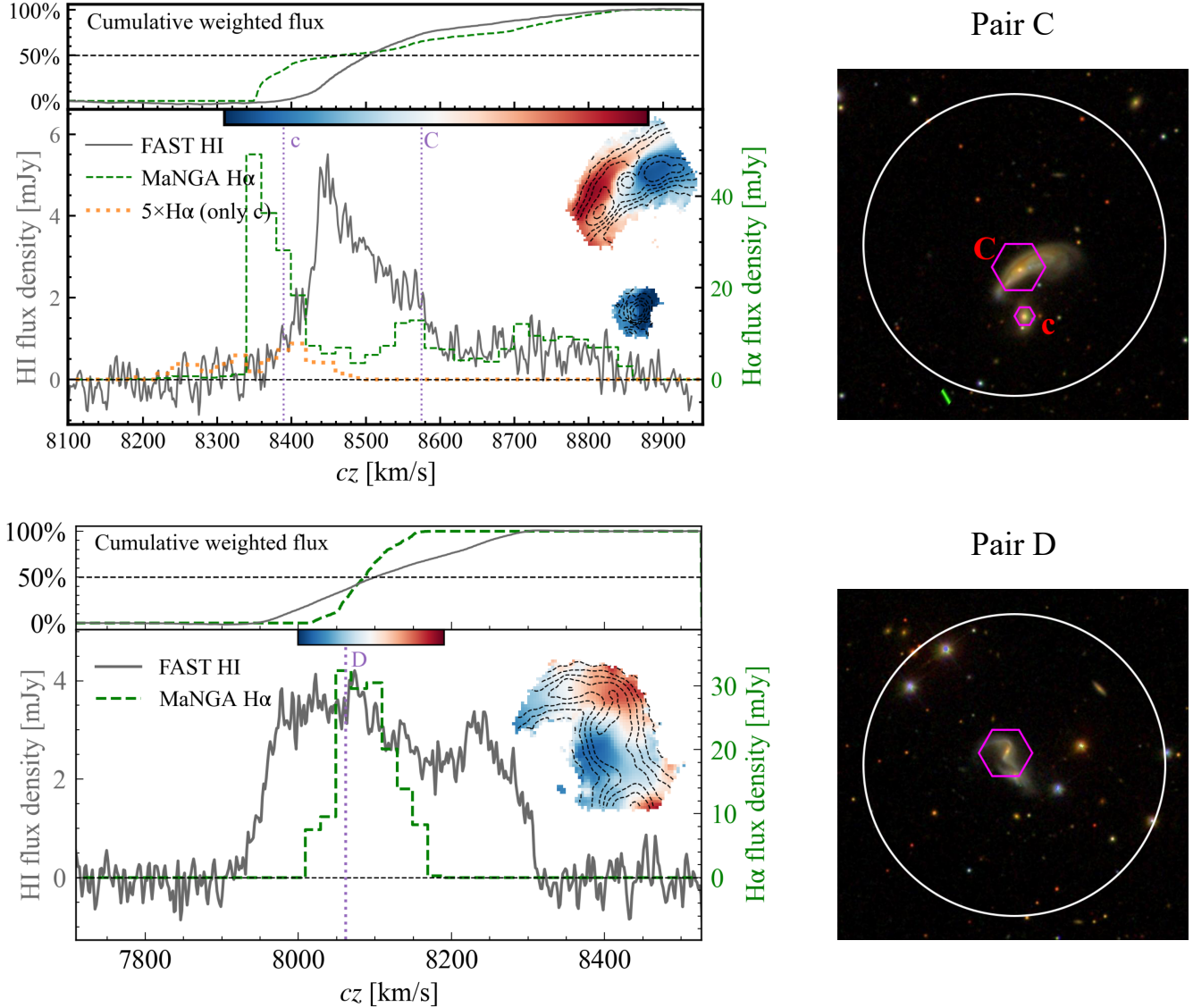


Figure 5. Same with 3. Galaxy c only has marginal contribution to the overall H α line profile of the pair system. In the upper panel, the H α profile from galaxy c is scaled up by a factor of five and plotted as the orange dotted line for a better demonstration. The majority of the H α emission of the system is from the upper right tail of the galaxy (bluer part).

compact ionized gas cores with different line-of-sight velocities.

Instead of a double-horn shape for typical rotational atomic disks, the H I line profile is centrally peaked. At the velocity of the southern nuclei ($\sim 2210 \text{ km s}^{-1}$), the H I also shows an excess hump, likely associated with the ionized gas. The line width of H I (225 km s^{-1}) is three times wider than the H α ($\sim 70 \text{ km s}^{-1}$, peak-to-peak), confirming the common understanding that the atomic gas is more spread out into the vicinity environment of the galaxy, than the ionized gas that is often bound inside the galaxy (Navarro et al. 1997). We note that the limited MaNGA IFU size for this system may cause the H α line width to be underestimated, but the H α velocity map already shows flattening in the northern and southern

region, indicating that the H α line is not likely to become as wide as the H I line even with enough IFU coverage.

4.7. Summary of the comparisons between the global H I and H α

In summary, the H I line profiles typically show one continuous component of linewidth between ~ 220 to 400 km s^{-1} in our sample. Wider H I line profile ($\sim 400 \text{ km s}^{-1}$) is found in pairs undergoing merging or just merged with distorted morphology (C, D, E, F), indicating that the merging process directly affects the atomic gas in their environment. The H α line profiles, despite the lower velocity resolution, often show velocity components peaking at one member galaxy or the center of the two member galax-

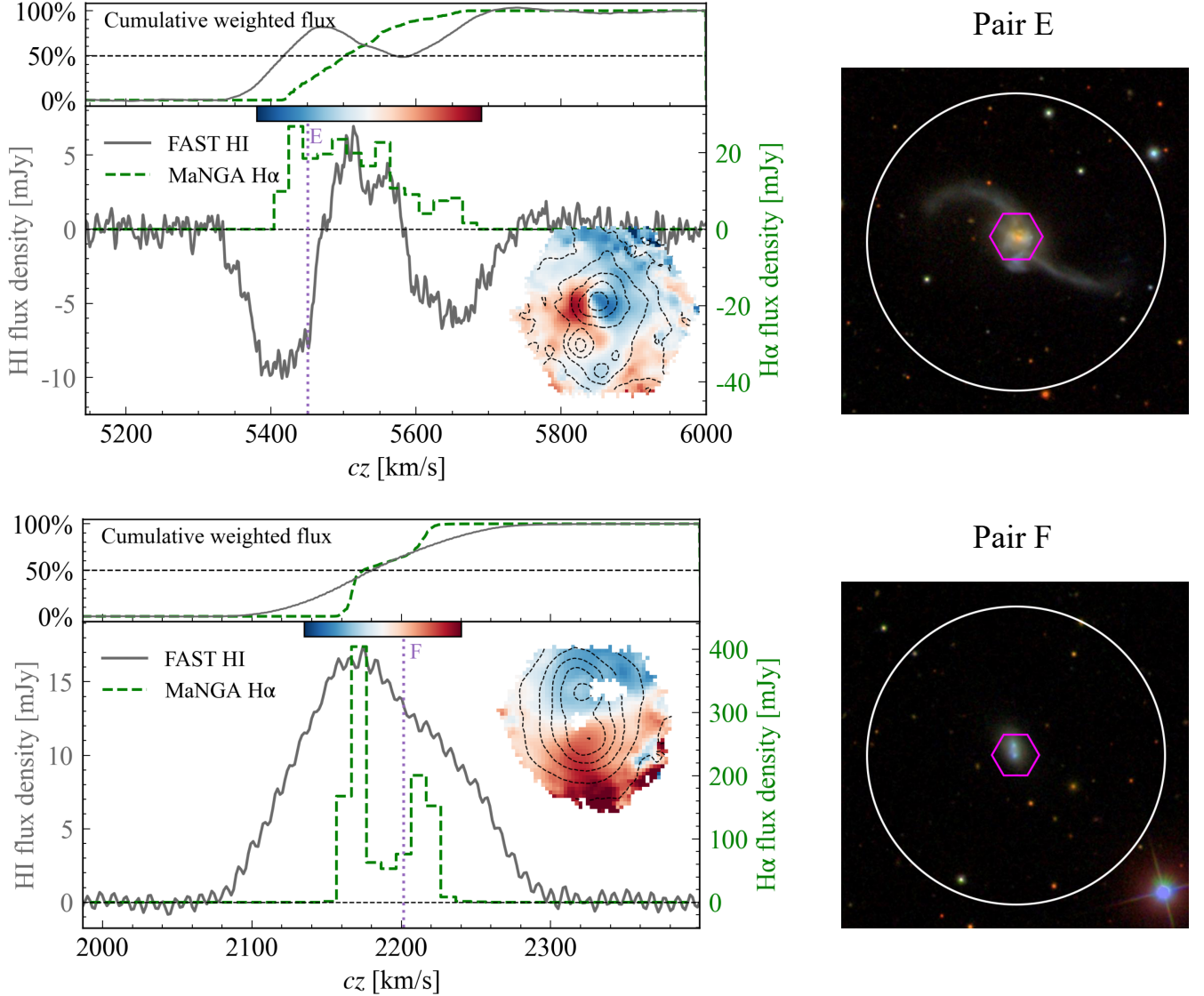


Figure 6. Same with 3, but for post-mergers E and F. Pair E show strong absorption features so that its cumulative H I flux is not monotonically increasing.

ies (A, C, D, F). In most cases, the H I velocity span covers both members, except in Pair A, where the HI profile is better aligned with one member galaxy. This SFG-SFG pair seems to be in the pre-merger case, when the galaxy interaction may not have started yet.

In isolated galaxies, the atomic and ionized gas have been found to share similar kinematics, and the line shape difference could be due to the clumpier H α distributions, as reported before in Andersen & Bershadsky (2009). Considering that the volatile merging process should affect the gas kinematics in the system, regardless of the gas scale or type (e.g. Schiminovich et al. 2013), it is possible that merging would eventually align the atomic and ionized gases.

From a global point of view, we notice that the 50% cumulative flux velocities are generally different between the H I

and H α emissions (Table 3). We note that given the different scales, distributions, and strengths of the ionized and atomic gases, it is normal that the widths, spans, and absolute values of the H I and H α emission line profiles are different. Therefore, we use Δv_{c50} , the differences between the bulk central velocities of the H I and H α emissions, as a proxy for the alignment level between the two gas contents. Lower Δv_{c50} values indicate better alignment, and vice versa. We notice that in the pre-merging case, Pair A, Δv_{c50} is $\sim 140 \text{ km s}^{-1}$, though we also note that one ionized gas spectrum does not have H I emission associated with it. As we move towards later merging cases, this value decreases from a few tens of km s^{-1} in merging cases (Pair C, D) to $<10 \text{ km s}^{-1}$ in the post-merger case (Pair F).

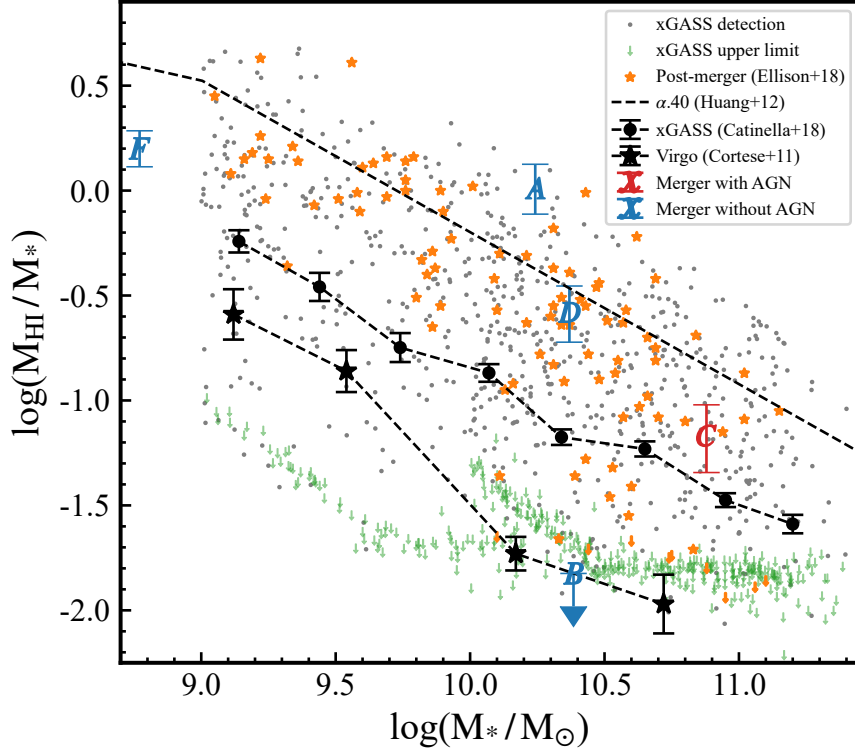


Figure 7. H I fraction versus stellar mass. We compare the pairs in this paper with statistic samples in different gas environments from large H I surveys, namely: H I-rich sample from ALFALFA survey (Huang et al. 2012); H I-normal sample from xGASS (Catinella et al. 2018); and H I-poor sample from the Virgo cluster (Cortese et al. 2011). The pair with AGN (C) lies along the H I-rich to H I-normal regions, while the pairs without AGNs (A, B, D, F) show a wider range of H I fractions, similar to the post merger sample (orange stars) in Ellison et al. (2018).

Despite our small sample size, this trend suggests that the atomic and ionized gas tend to share similar kinematic centers toward later merging stages. This is consistent with the scenario that the merging process would eventually align and settle the different gas contents down to a common central velocity, possibly as a manifestation of gas concentration.

The overall line profiles of H I and H α are generally different in all pairs in our sample, except for Pair C, in which part of the spectra show some level of overlap. Our results are in general agreement with previous studies that illustrated the environment impact on gases of different phases. For the atomic gas, galaxy merger or a dense environment can increase the asymmetry of the spatial distributions (Angiras et al. 2006, 2007), which has also been confirmed in ionized gases by several spatially resolved studies (e.g. Feng et al. 2020; Bagge et al. 2023).

5. H I SCALING RELATIONS

In this section, we investigate the H I mass properties of the six pairs, and compare them to the scaling relations derived from large samples of field galaxies. We note that because the H I observations do not resolve the pair members, the H I mass, stellar mass, and SFR used in this section are the integrated values for pair system as a whole.

The H I fraction, defined as $\log(M_{\text{HI}}/M_*)$, is used to estimate the atomic gas abundance of a galaxy. The H I frac-

tion has been widely reported to have a negative correlation with the stellar mass (see Saintonge & Catinella 2022, for a review), also known as the H I scaling relation. However, the H I scaling relation is found to depend on the survey depth of the derived sample, therefore with different values in the literature. In Fig. 7, we compare our mergers with the extended GALEX Arcicibo SDSS Survey (xGASS, Catinella et al. 2018) representative sample (gray dots and green upper-limits), as well as the scaling relation derived from several other surveys. The dashed line is the scaling relation from the 40% ALFALFA survey (Huang et al. 2012), which is mostly a local H I-rich sample. The dashed line with solid circles and errors is from a deeper H I survey, xGASS. This scaling relation includes H I non-detections, so can serve as a prediction of H I-normal galaxies. The dashed-star line is the relation from the galaxies in the Virgo cluster (Cortese et al. 2011), representative of the H I-poor galaxies in dense environments.

The pair systems with AGNs located near the average of the xGASS survey, indicating they are H I-normal systems, while the SFG mergers show a wide range of H I fraction. The upper-limit SFG pair, Pair B, is a H I-poor system. Here we do not include the analysis for Pair E, since its H I mass is not constrained due to strong absorption.

The atomic gas star formation efficiency (SFE), defined as $\text{SFE} = \text{SFR}/M_{\text{HI}}$, is a proxy of how efficient the galaxy

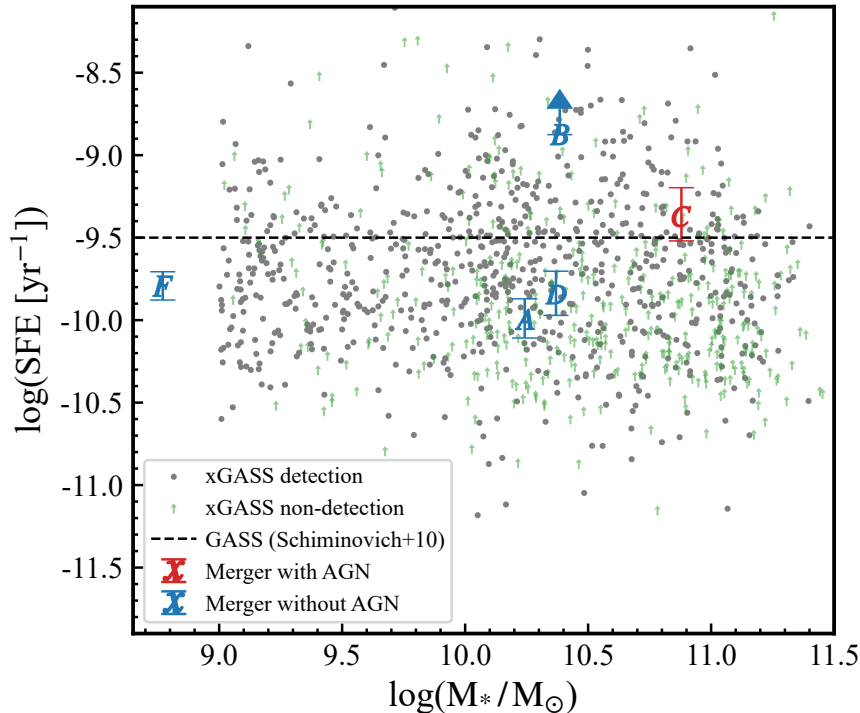


Figure 8. The atomic gas star-formation efficiency versus stellar mass. Compared to the xGASS survey (gray dots and green lower limits), the five H I-detected pairs locate in normal SFE range. The non-detection pair B has relatively high star-formation efficiency. The black dashed line shows the average value of the xGASS survey sample.

can convert the atomic gas to stars. Previous H I surveys have shown that the atomic gas SFE does not significantly evolve with the stellar mass, and has an almost constant average value of $\sim 10^{-9.5} \text{ yr}^{-1}$ (Schiminovich et al. 2010). Some studies also investigate the impact of merger on atomic gas SFE. For instance, Zuo et al. (2018) showed that the spiral-spiral galaxy pairs have higher SFE than spiral-elliptical pairs, Yu et al. (2022b) found higher SFE during the galaxy-galaxy pericentric passage.

As shown in Fig. 8, with and without AGN, the pair systems do not deviate significantly from the xGASS sample. For Pair B without HI detection, the lower limit of SFE is already $\sim 1\sigma$ (~ 0.5 dex) higher than the average value of the xGASS detected sample. Considering that the molecular gas is also associated with ongoing star formation activities (e.g. Lin et al. 2019), future CO observations would be useful to confirm the star formation efficiency and possibly the location of the star formation activities. On the other hand, the other three SFG pairs (A, D, F), lie about 0.3-0.6 dex below the average. This agrees with a scenario that during the galaxy merger, the atomic gas fraction enhancement is more significant compared to the SFR enhancement. A similar phenomenon is also observed for several post-merger samples (e.g., Ellison et al. 2018), but we need a larger sample to confirm this.

6. SUMMARY

This paper presents case studies of comparing optical IFU and single-dish radio telescope observations between the H α and H I emission line profiles in galaxy mergers. We use the FAST telescope to observe the H I for a small sample of six galaxy pairs at different merger stages and of different nuclear activities. Five systems are detected with secure H I emissions. Their H I line profiles all show irregular shapes, such as broadening, asymmetric peaks, and absorption features, which is consistent with archival H I observations on galaxy mergers (e.g. Zuo et al. 2022), and addresses mergers' strong disturbances on the atomic gas. We do not find galaxy pairs at any stage showing two separable H I emission lines in the spectra.

We construct the global H α line profiles from MaNGA IFU data and compare them with the H I line profiles, as a direct approach to compare the ionized gas and the atomic gas. In summary, the line widths and line profile shapes of H I and H α are different in all the five H I-detected galaxy pairs, suggesting that the disturbance of galaxy merger may have different impacts on the atomic and ionized gases, resulting in unique gas distributions. Along the line-of-sight velocities, however, some peaks or broadening features in the two profiles can match with each other, which is indirect evidence that the ionized and atomic gas have correlation in at least certain regions. The line-of-sight velocity offsets between the H I and H α emission line centers (Δv_{c50}), shows a decreasing trend toward later merging stages. This tendency indicates that the merging process may contribute to the mix-

ing and eventually align the atomic and ionized gas contents to the same velocity centers. Larger statistical samples are needed to verify this scenario.

The H I fraction and atomic gas SFE of these six pair systems cover wide parameter spaces, and all lie within the 3σ scatter of the large sample results. We do not find evidence that merger or AGN activities have significant impact on the amount of galaxies' atomic gas.

Compared to the radio interferometry observations, combining optical IFUs and single-dish radio telescope is an efficient way to study the relative properties of the ionized and atomic gas in galaxies, but this method was only applied in a few works (e.g. Andersen et al. 2006; Andersen & Bershadsky 2009; Watts et al. 2023). We expect new, larger statistical samples with both optical IFU and H I observations to study the size, radial distribution, and rotation angle of the atomic gas, and the method presented in this work could serve as an alternative way to analyze the kinematics and distribution of gas contents of different origins and scales in complex systems like the mergers and pairs.

The authors thank the anonymous referees for their constructive comments and suggestions. We would like to thank Ningyu Tang, Yingjie Jing for their suggestions and help on FAST data reduction. We also thank the MaNGA DAP team and NSA team for providing the datacubes and catalogs. This work is sponsored by the National Key R&D Program of China (MOST) for grant No. 2022YFA1605300, the National Nature Science Foundation of China (NSFC) grants No. 12273051 and 11933003. Support for this work is also partly provided by the CASSACA. This work made use of the data from FAST (Five-hundred-meter Aperture Spherical radio Telescope). FAST is a Chinese national mega-science facility, operated by National Astronomical Observatories, Chinese Academy of Sciences. Funding for the Sloan Digital Sky Survey IV has been provided by the Alfred P. Sloan Foundation, the U.S. Department of Energy Office of Science, and the Participating Institutions. SDSS-IV acknowledges support and resources from the Center for High-Performance Computing at the University of Utah. The SDSS website is www.sdss.org. SDSS-IV is managed by the Astrophysical Research Consortium for the Participating Institutions of the SDSS Collaboration including the Brazilian Participation Group, the Carnegie Institution for Science, Carnegie Mellon University, the Chilean Participation Group, the French Participation Group, Harvard-Smithsonian Center for Astrophysics, Instituto de Astrofísica de Canarias, The Johns Hopkins University, Kavli Institute for the Physics and Mathematics of the Universe (IPMU) / University of Tokyo, the Korean Participation Group, Lawrence Berkeley National Laboratory, Leibniz Institut für Astrophysik Potsdam (AIP), Max-Planck-Institut für Astronomie (MPIA Heidelberg), Max-Planck-Institut für Astrophysik (MPA Garching), Max-Planck-Institut für Extraterrestrische Physik (MPE), National Astronomical Observatories of China, New Mexico State University, New York University, University of Notre Dame, Observatório Nacional / MCTI, The Ohio State University, Pennsylvania State University, Shanghai Astronomical Observatory, United Kingdom Participation Group, Universidad Nacional Autónoma de México, University of Arizona, University of Colorado Boulder, University of Oxford, University of Portsmouth, University of Utah, University of Virginia, University of Washington, University of Wisconsin, Vanderbilt University, and Yale University.

Facilities: FAST (Jiang et al. 2019), SDSS 2.5 m (Gunn et al. 2006)

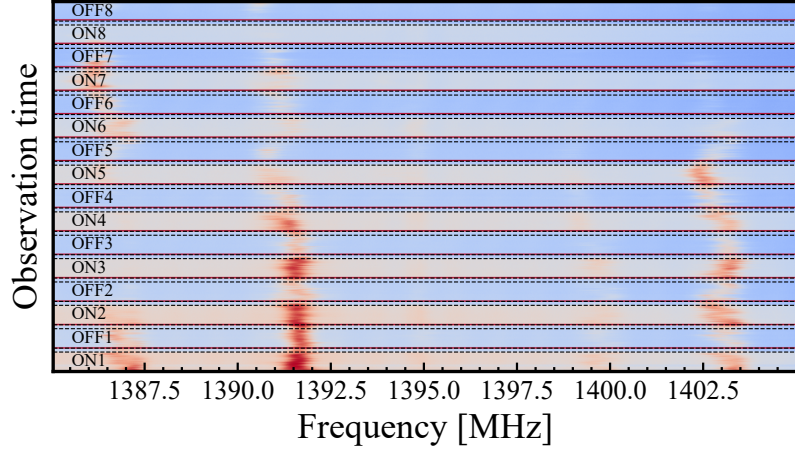
Software: Astropy (Astropy Collaboration et al. 2013, 2018)

APPENDIX

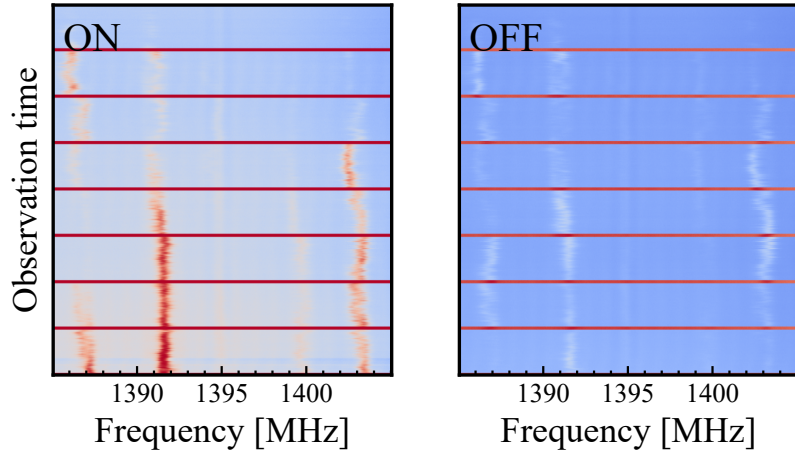
A. FAST DATA REDUCTION AND CALIBRATION FOR ON/OFF MODE

We adopt and modify the data reduction and calibration procedure from Jiang et al. (2020) and Cheng et al. (2020).

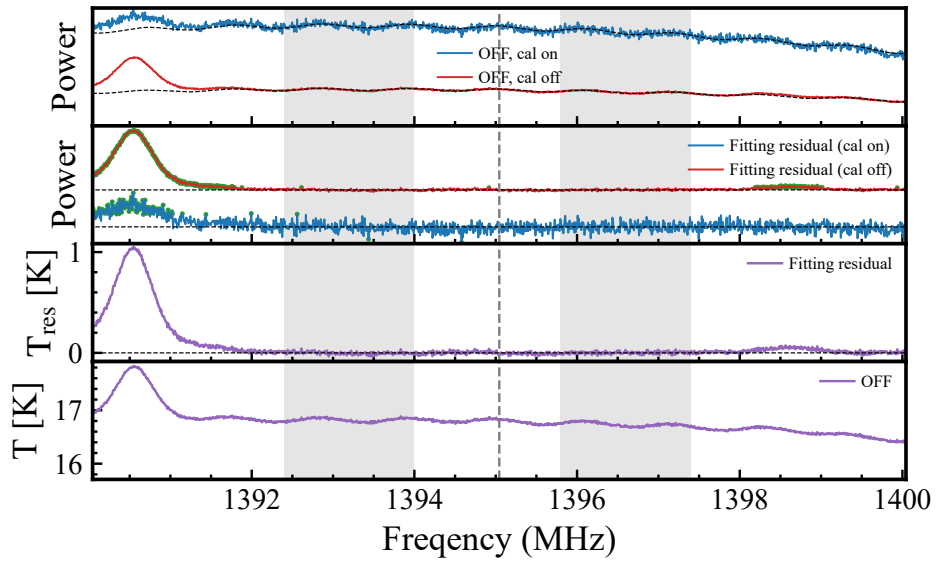
We summarize and illustrate the procedure in Fig. A1, and is described as follows:



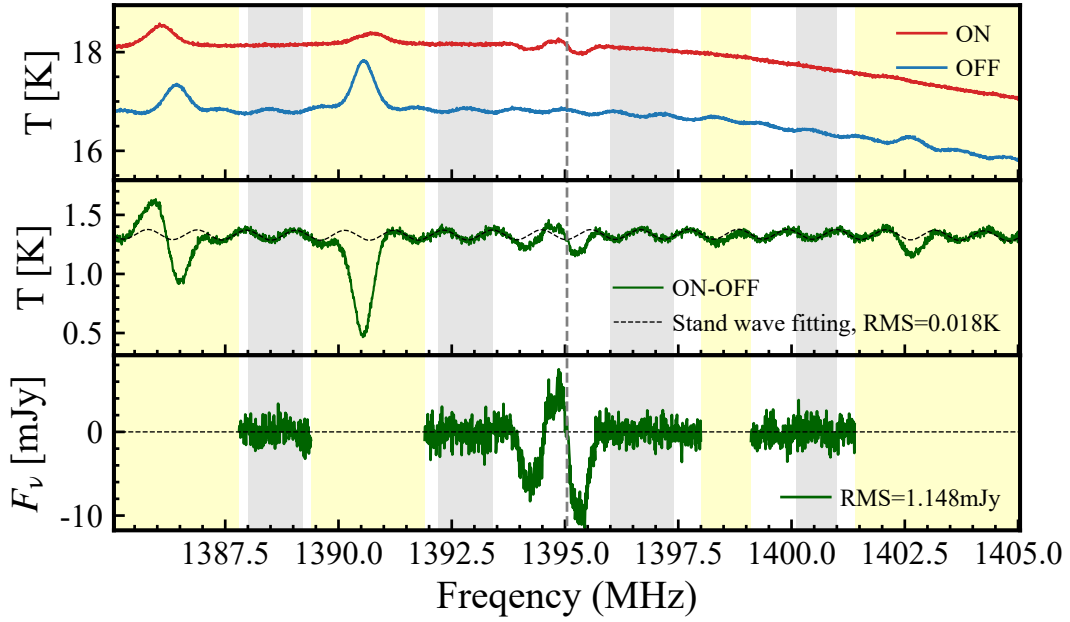
(a)



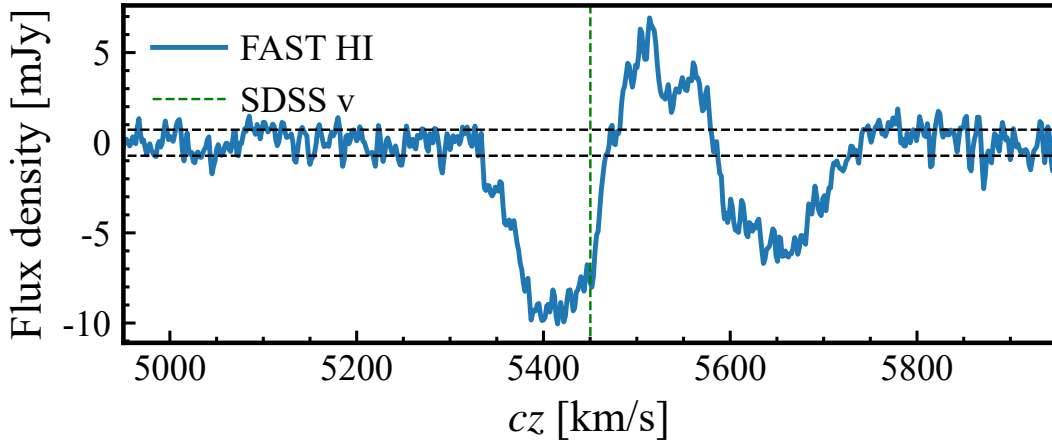
(b)



(c)



(d)



(e)

Figure A1. The data reduction procedure adopted in this work, using the data from Pair E as an illustration. **Step 1 (a):** The ‘waterfall’ map of the raw data in a 16 MHz frequency range. The crimson signals are the RFIs and calibration noises. **Step 2 (b):** The ‘waterfall’ maps of combined ON or OFF observations after removing the time domain RFIs (if exist). **Step 3 (c):** Example temperature calibration of a 5-minutes OFF-target observation. The gray backgrounds are the selected frequency range with no spectra features used for baseline fitting, and the gray dashed line in the center marks the expected H I frequency from the optical redshift. Panel 1 and 2 are the noise-on (red) and noise-off (blue) spectra before and after baseline (black curves in panel 1) removal. Green dots in panel 2 mark the possible RFI frequencies. Black lines in panel 2 and 3 mark the zero point baseline. As a check, panel 3 shows the resulting temperature profile (purple) combining the noise-on and noise-off observations. Panel 4 is the combined noise-off and noise-on spectra to be used in the next step, after converting the counts into temperatures. **Step 4 (d):** Get the H I spectra (lower panel) from each set of neighboring ON and OFF observations derived in (c). Baseline is fitted (black dashed lines) and removed. Yellow strips mask the frequency range heavily affected by the RFI, and these frequency regions are not used for baseline fitting. **Step 5 (e):** Stacking all H I spectra derived in (d) as the final result. The weight of each exposure is calculated by the rms in the featureless gray zones.

1. Remove the time-domain RFIs: We find that the RFIs can be divided into two types, the time-domain RFIs (hereafter t-RFIs) and the frequency-domain RFIs (hereafter f-RFIs). Usually, the t-RFIs are strong and will appear or disappear relatively abruptly. The f-RFIs usually appear continuously in a narrow frequency range of several MHz, and are weaker than the t-RFIs, thus we will remove the f-RFIs by masking relative frequencies later in step 3. In the first step, we manually identify and remove the t-RFIs by their strong fluxes, as shown in Fig. A1(a). In this way, we get the ON/OFF spectra not affected by t-RFIs, as shown in Fig. A1(b).

2. Temperature calibration: As mentioned in Sec 3.1, the calibration noise is injected during the first 20 seconds of each ON and each OFF exposure. For each 16 MHz frequency bandpass, the antenna temperature profile is calculated as:

$$T_{\text{noise,off}}(\nu) = T_{\text{noise,inj}}(\nu) \times \frac{f_{\text{noise,off}}(\nu)}{f_{\text{noise,on}}(\nu) - \bar{f}_{\text{noise,off}}(\nu)}, \quad (\text{A1})$$

where $T_{\text{noise,inj}}(\nu)$ is the injected noise temperature in Kelvin, $T_{\text{noise,off}}$ is temperature with no injected noise, sometimes referred to the antenna Temperature, $f_{\text{noise,off}}(\nu)$ is the mean digital counts strengths as a function of frequency in the noise off mode, and $\bar{f}_{\text{noise,off}}$ is the mean digital counts strengths in the selected frequency ranges, for noise on and noise off, respectively. In our observations, we use the noise diode noise temperature profile, which was reported to have a temperature varying around 5.4K for the adopted ‘high power’ injected calibration noise at the time of observation (see Section 3.1 of Jiang et al. 2020). The choice of averaging the $\bar{f}_{\text{noise,off}}$ is to reduce the influences of f-RFIs and signals on the temperature calibration. In this step, we carefully avoid the regions with possible f-RFI signals (as marked in green in Fig. A1(c), panel 3, see below).

In our calibration frequency range of ~ 16 MHz, the baseline is dominated by the stable standing wave with a ~ 1 MHz period, thus can be fitted by a polynomial plus a sinusoidal function. As shown in Fig. A1(c), we calculate the $\bar{f}(\nu)$ by fitting a (polynomial+sinusoidal) baseline profile to the spectra in the frequency ranges (gray stripes) that are least affected by signals or f-RFIs. The top two panels show the spectra for noise on (blue) and noise off (red) modes before and after removing the fitted baseline; while the bottom two panels show the resulting $T_{\text{noise,off}}(\nu)$ after and before removing the fitted baseline profile. In addition, if the OFF spectra in noise-off mode at the expected H I frequency still show residual values after the baseline removal, we mask the exposure as ‘failed calibration’ and exclude it from the stacking in the next step, to make sure that OFF observations can serve as ‘no flux’ reference. This only applies to a few exposures.

3. Obtain the spectra from each ON observation: As shown in Fig. A1(d), we select the contiguous OFF spectrum (red, T_{OFF}) as the baseline for each ON observation (blue, T_{ON}). Then we follow Equation A2 to obtain the spectra

(green spectrum in middle panel) for baseline fitting and f-RFI removing.

$$T_{\text{HI}}(\nu) = T_{\text{OFF}}(\nu) \times \frac{T_{\text{ON}}(\nu) - T_{\text{OFF}}(\nu)}{T_{\text{OFF}}}, \quad (\text{A2})$$

Middle panel of Fig. A1(d) shows the ON-OFF spectra, where the yellow strips are the masked out f-RFI frequency regions, the light gray strips are the featureless regions used for baseline fitting. The standing wave baseline is then fitted in these featureless regions using a polynomial+sinusoidal profile, as plotted in black lines in the middle panel. The standing wave is caused by the reflection between the receiver and the mirror panels, thus has a period of ~ 1 MHz (~ 300 meter/ c). For reliability, we make sure that the baseline fitting frequency regions span at least ~ 4 MHz (>4 sinusoidal periods). The green spectrum in the lower panel is the residual spectra after removing the fitted baseline and masking out f-RFI regions, i.e. the H I spectrum for one set of ON observations. The temperature are then converted to flux density using the gain profile at the targeted frequencies (Jiang et al. 2020), which varies around 16.0 K Jy^{-1} for all of our targets. When the zenith angle of the source is higher than 26.4° , the effective aperture of FAST become smaller, resulting in a lower gain. We correct the gain based on the test in Jiang et al. (2020) in this step. We derive the spectrum for each ON exposure first, because during each 40 minutes observations, the system temperature and the gain of FAST receiver varies. The rms are calculated from the residual in the featureless gray zones.

4. Spectra stacking and H I mass: After we obtain the ON-OFF spectra of all the ON exposures for the same target, we stack the baseline-removed spectra, weighted by their rms. Then the spectra are Hanning-smoothed to a velocity resolution of $\sim 3.3 \text{ km s}^{-1}$ as our final results. The H I spectra of the six pairs are shown in Fig. 2. We find five H I detections with high S/N and one non-detection with low rms to restrict the upper limit of H I mass (Pair B). Green dashed line(s) show the optical redshift(s) of the member galaxies, and red dashed line corresponds to the center of the detected H I emission line.

B. THE SENSITIVITY OF FAST: COMPARED TO GBT AND ARECIBO

The sensitivity of a single-dish telescope is proportionate to the square of the aperture diameter and also depends on the system temperature. Here we compare the sensitivity of our FAST observation with the GBT and Arecibo observations when using the ON-OFF mode to observe emission lines. For GBT observations, we use the result of the H I-MaNGA survey. For Arecibo observations, we use the results from the GASS survey. They both used the ON-OFF observation mode and share similar data reduction methods with this paper, thus are suitable for comparing the sensitivity. For their observation setting-ups and data reduction, we refer the readers to Masters et al. (2019) and Catinella et al. (2010), respectively.

Here we use the rms when the velocity resolution is converted to 10 km s^{-1} to compare the sensitivity of different telescopes. Ideally, the rms of an observation can be expressed as: $\text{rms} \propto t^{-0.5} \times \text{dv}^{0.5}$. At given integration time and velocity resolution, lower rms means higher sensitivity. In Fig. B1, we plot the rms versus integration time of the observations from different telescopes. The blue dots, green dots and red stars are the GBT, Arecibo, and FAST observations, respectively. The black line is the relation used for estimating the rms of a GBT observation. We also plot the $0.3 \times$ of the relation as the black-dashed line to guide the eyes

for comparison. For shorter time observations, the sensitivity of FAST is $\sim 5 \times$ better than that of GBT, and $\sim 2 \times$ than that of Arecibo. For long-time exposure, however, the rms of FAST observation does not significantly decrease following the theoretical predication. This phenomenon was also found in Cheng et al. (2020). One possible reason is found during our data reduction, that the RFI can increase the system temperature, resulting in higher rms. This is the performance of FAST at the date of early 2021. Future improvements are needed for FAST to suppress the rms for long-time spectral line observation mode.

REFERENCES

- Abdurro'uf, Accetta, K., Aerts, C., et al. 2022, *ApJS*, 259, 35, doi: [10.3847/1538-4365/ac4414](https://doi.org/10.3847/1538-4365/ac4414)
- Andersen, D. R., & Bershadly, M. A. 2009, *ApJ*, 700, 1626, doi: [10.1088/0004-637X/700/2/1626](https://doi.org/10.1088/0004-637X/700/2/1626)
- Andersen, D. R., Bershadly, M. A., Sparke, L. S., et al. 2006, *ApJS*, 166, 505, doi: [10.1086/506609](https://doi.org/10.1086/506609)
- Angiras, R. A., Jog, C. J., Dwarakanath, K. S., & Verheijen, M. A. W. 2007, *MNRAS*, 378, 276, doi: [10.1111/j.1365-2966.2007.11779.x](https://doi.org/10.1111/j.1365-2966.2007.11779.x)
- Angiras, R. A., Jog, C. J., Omar, A., & Dwarakanath, K. S. 2006, *MNRAS*, 369, 1849, doi: [10.1111/j.1365-2966.2006.10418.x](https://doi.org/10.1111/j.1365-2966.2006.10418.x)
- Astropy Collaboration, Robitaille, T. P., Tollerud, E. J., et al. 2013, *A&A*, 558, A33, doi: [10.1051/0004-6361/201322068](https://doi.org/10.1051/0004-6361/201322068)
- Astropy Collaboration, Price-Whelan, A. M., Sipőcz, B. M., et al. 2018, *AJ*, 156, 123, doi: [10.3847/1538-3881/aabc4f](https://doi.org/10.3847/1538-3881/aabc4f)
- Bagge, R. S., Foster, C., Battisti, A., et al. 2023, *PASA*, 40, e060, doi: [10.1017/pasa.2023.58](https://doi.org/10.1017/pasa.2023.58)
- Barnes, J. E., & Hernquist, L. 1992, *ARA&A*, 30, 705, doi: [10.1146/annurev.aa.30.090192.003421](https://doi.org/10.1146/annurev.aa.30.090192.003421)
- . 1996, *ApJ*, 471, 115, doi: [10.1086/177957](https://doi.org/10.1086/177957)
- Belfiore, F., Westfall, K. B., Schaefer, A., et al. 2019, *AJ*, 158, 160, doi: [10.3847/1538-3881/ab3e4e](https://doi.org/10.3847/1538-3881/ab3e4e)
- Bigiel, F., Leroy, A., Walter, F., et al. 2008, *AJ*, 136, 2846, doi: [10.1088/0004-6256/136/6/2846](https://doi.org/10.1088/0004-6256/136/6/2846)
- Blanton, M. R., & Roweis, S. 2007, *AJ*, 133, 734, doi: [10.1086/510127](https://doi.org/10.1086/510127)
- Bok, J., Blyth, S. L., Gilbank, D. G., & Elson, E. C. 2019, *MNRAS*, 484, 582, doi: [10.1093/mnras/sty3448](https://doi.org/10.1093/mnras/sty3448)
- Bundy, K., Bershadly, M. A., Law, D. R., et al. 2015, *ApJ*, 798, 7, doi: [10.1088/0004-637X/798/1/7](https://doi.org/10.1088/0004-637X/798/1/7)
- Cardelli, J. A., Clayton, G. C., & Mathis, J. S. 1989, *ApJ*, 345, 245, doi: [10.1086/167900](https://doi.org/10.1086/167900)
- Catinella, B., Schiminovich, D., Kauffmann, G., et al. 2010, *MNRAS*, 403, 683, doi: [10.1111/j.1365-2966.2009.16180.x](https://doi.org/10.1111/j.1365-2966.2009.16180.x)
- Catinella, B., Saintonge, A., Janowiecki, S., et al. 2018, *MNRAS*, 476, 875, doi: [10.1093/mnras/sty089](https://doi.org/10.1093/mnras/sty089)
- Cheng, C., Ibar, E., Du, W., et al. 2020, *A&A*, 638, L14, doi: [10.1051/0004-6361/202038483](https://doi.org/10.1051/0004-6361/202038483)
- Cortese, L., Catinella, B., Boissier, S., Boselli, A., & Heinis, S. 2011, *MNRAS*, 415, 1797, doi: [10.1111/j.1365-2966.2011.18822.x](https://doi.org/10.1111/j.1365-2966.2011.18822.x)
- Dai, Y. S., Malkan, M. M., Teplitz, H. I., et al. 2021, *ApJ*, 923, 156, doi: [10.3847/1538-4357/ac2f96](https://doi.org/10.3847/1538-4357/ac2f96)
- Davies, R. L., Groves, B., Kewley, L. J., et al. 2017, *MNRAS*, 470, 4974, doi: [10.1093/mnras/stx1559](https://doi.org/10.1093/mnras/stx1559)
- Ellison, S. L., Brown, T., Catinella, B., & Cortese, L. 2019, *MNRAS*, 482, 5694, doi: [10.1093/mnras/sty3139](https://doi.org/10.1093/mnras/sty3139)
- Ellison, S. L., Catinella, B., & Cortese, L. 2018, *MNRAS*, 478, 3447, doi: [10.1093/mnras/sty1247](https://doi.org/10.1093/mnras/sty1247)
- Ellison, S. L., Patton, D. R., Simard, L., & McConnachie, A. W. 2008, *AJ*, 135, 1877, doi: [10.1088/0004-6256/135/5/1877](https://doi.org/10.1088/0004-6256/135/5/1877)
- Fabian, A. C. 2012, *ARA&A*, 50, 455, doi: [10.1146/annurev-astro-081811-125521](https://doi.org/10.1146/annurev-astro-081811-125521)
- Feng, S., Shen, S.-Y., Yuan, F.-T., Riffel, R. A., & Pan, K. 2020, *ApJL*, 892, L20, doi: [10.3847/2041-8213/ab7dba](https://doi.org/10.3847/2041-8213/ab7dba)
- Geréb, K., Maccagni, F. M., Morganti, R., & Oosterloo, T. A. 2015, *A&A*, 575, A44, doi: [10.1051/0004-6361/201424655](https://doi.org/10.1051/0004-6361/201424655)
- Giovanelli, R., Haynes, M. P., Kent, B. R., et al. 2005, *AJ*, 130, 2598, doi: [10.1086/497431](https://doi.org/10.1086/497431)
- Gunn, J. E., & Gott, J. Richard, I. 1972, *ApJ*, 176, 1, doi: [10.1086/151605](https://doi.org/10.1086/151605)
- Gunn, J. E., Siegmund, W. A., Mannery, E. J., et al. 2006, *AJ*, 131, 2332, doi: [10.1086/500975](https://doi.org/10.1086/500975)
- He, C., Xu, C. K., Domingue, D., Cao, C., & Huang, J.-s. 2022, *ApJS*, 261, 34, doi: [10.3847/1538-4365/ac73ec](https://doi.org/10.3847/1538-4365/ac73ec)
- Hibbard, J. E., Vacca, W. D., & Yun, M. S. 2000, *AJ*, 119, 1130, doi: [10.1086/301263](https://doi.org/10.1086/301263)
- Hibbard, J. E., & van Gorkom, J. H. 1996, *AJ*, 111, 655, doi: [10.1086/117815](https://doi.org/10.1086/117815)
- Hopkins, P. F., Hernquist, L., Cox, T. J., & Kereš, D. 2008, *ApJS*, 175, 356, doi: [10.1086/524362](https://doi.org/10.1086/524362)
- Huang, S., Haynes, M. P., Giovanelli, R., & Brinchmann, J. 2012, *ApJ*, 756, 113, doi: [10.1088/0004-637X/756/2/113](https://doi.org/10.1088/0004-637X/756/2/113)

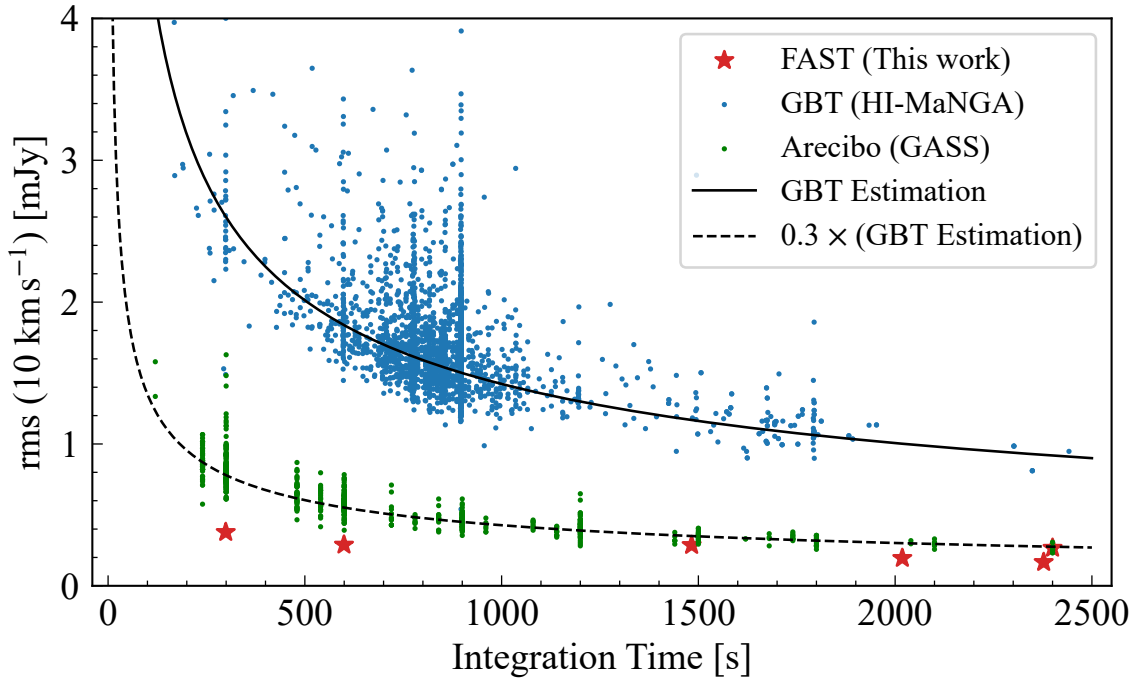


Figure B1. The rms versus integration times from HI-MaNGA survey (blue dots), GASS survey (green dots), and our FAST observations (red stars). All the rms value are corrected to the velocity resolution of 10 km s^{-1} .

Hwang, H. S., Elbaz, D., Dickinson, M., et al. 2011, *A&A*, 535, A60, doi: [10.1051/0004-6361/201117476](https://doi.org/10.1051/0004-6361/201117476)

Iono, D., Yun, M. S., & Ho, P. T. P. 2005, *ApJS*, 158, 1, doi: [10.1086/429093](https://doi.org/10.1086/429093)

Jiang, P., Yue, Y., Gan, H., et al. 2019, *Science China Physics, Mechanics, and Astronomy*, 62, 959502, doi: [10.1007/s11433-018-9376-1](https://doi.org/10.1007/s11433-018-9376-1)

Jiang, P., Tang, N.-Y., Hou, L.-G., et al. 2020, *Research in Astronomy and Astrophysics*, 20, 064, doi: [10.1088/1674-4527/20/5/64](https://doi.org/10.1088/1674-4527/20/5/64)

Jin, G., Dai, Y. S., Pan, H.-A., et al. 2021, *ApJ*, 923, 6, doi: [10.3847/1538-4357/ac2901](https://doi.org/10.3847/1538-4357/ac2901)

Kennicutt, R. C., & Evans, N. J. 2012, *ARA&A*, 50, 531, doi: [10.1146/annurev-astro-081811-125610](https://doi.org/10.1146/annurev-astro-081811-125610)

Kroupa, P. 2001, *MNRAS*, 322, 231, doi: [10.1046/j.1365-8711.2001.04022.x](https://doi.org/10.1046/j.1365-8711.2001.04022.x)

Law, D. R., Westfall, K. B., Bershad, M. A., et al. 2021, *AJ*, 161, 52, doi: [10.3847/1538-3881/abcaa2](https://doi.org/10.3847/1538-3881/abcaa2)

Lin, L., Koo, D. C., Weiner, B. J., et al. 2007, *ApJL*, 660, L51, doi: [10.1086/517919](https://doi.org/10.1086/517919)

Lin, L., Pan, H.-A., Ellison, S. L., et al. 2019, *ApJL*, 884, L33, doi: [10.3847/2041-8213/ab4815](https://doi.org/10.3847/2041-8213/ab4815)

Lin, X., Wang, J., Kilborn, V., et al. 2023, *ApJ*, 956, 148, doi: [10.3847/1538-4357/accea2](https://doi.org/10.3847/1538-4357/accea2)

Martin, D. C., Fanson, J., Schiminovich, D., et al. 2005, *ApJL*, 619, L1, doi: [10.1086/426387](https://doi.org/10.1086/426387)

Masters, K. L., Stark, D. V., Pace, Z. J., et al. 2019, *MNRAS*, 488, 3396, doi: [10.1093/mnras/stz1889](https://doi.org/10.1093/mnras/stz1889)

Nan, R. 2006, *Science in China: Physics, Mechanics and Astronomy*, 49, 129, doi: [10.1007/s11433-006-0129-9](https://doi.org/10.1007/s11433-006-0129-9)

Navarro, J. F., Frenk, C. S., & White, S. D. M. 1997, *ApJ*, 490, 493, doi: [10.1086/304888](https://doi.org/10.1086/304888)

Osterbrock, D. E., & Ferland, G. J. 2006, *Astrophysics of gaseous nebulae and active galactic nuclei* (Sausalito, Calif. : University Science Books)

Pan, H.-A., Lin, L., Hsieh, B.-C., et al. 2019, *ApJ*, 881, 119, doi: [10.3847/1538-4357/ab311c](https://doi.org/10.3847/1538-4357/ab311c)

Patton, D. R., Ellison, S. L., Simard, L., McConnachie, A. W., & Mendel, J. T. 2011, *MNRAS*, 412, 591, doi: [10.1111/j.1365-2966.2010.17932.x](https://doi.org/10.1111/j.1365-2966.2010.17932.x)

Pritchard, J. R., & Loeb, A. 2012, *Reports on Progress in Physics*, 75, 086901, doi: [10.1088/0034-4885/75/8/086901](https://doi.org/10.1088/0034-4885/75/8/086901)

Renzini, A., & Peng, Y.-j. 2015, *ApJL*, 801, L29, doi: [10.1088/2041-8205/801/2/L29](https://doi.org/10.1088/2041-8205/801/2/L29)

Roberts, M. S. 1975, *Radio Observations of Neutral Hydrogen in Galaxies* (University of Chicago Press), 309

Saintonge, A., & Catinella, B. 2022, *ARA&A*, 60, 319, doi: [10.1146/annurev-astro-021022-043545](https://doi.org/10.1146/annurev-astro-021022-043545)

Saintonge, A., Catinella, B., Tacconi, L. J., et al. 2017, *ApJS*, 233, 22, doi: [10.3847/1538-4365/aa97e0](https://doi.org/10.3847/1538-4365/aa97e0)

Schiminovich, D., van Gorkom, J. H., & van der Hulst, J. M. 2013, *AJ*, 145, 34, doi: [10.1088/0004-6256/145/2/34](https://doi.org/10.1088/0004-6256/145/2/34)

- Schiminovich, D., Catinella, B., Kauffmann, G., et al. 2010, MNRAS, 408, 919, doi: [10.1111/j.1365-2966.2010.17210.x](https://doi.org/10.1111/j.1365-2966.2010.17210.x)
- Smee, S. A., Gunn, J. E., Uomoto, A., et al. 2013, AJ, 146, 32, doi: [10.1088/0004-6256/146/2/32](https://doi.org/10.1088/0004-6256/146/2/32)
- Tumlinson, J., Peebles, M. S., & Werk, J. K. 2017, ARA&A, 55, 389, doi: [10.1146/annurev-astro-091916-055240](https://doi.org/10.1146/annurev-astro-091916-055240)
- Watts, A. B., Catinella, B., Cortese, L., Power, C., & Ellison, S. L. 2021, MNRAS, 504, 1989, doi: [10.1093/mnras/stab1025](https://doi.org/10.1093/mnras/stab1025)
- Watts, A. B., Cortese, L., Catinella, B., et al. 2023, MNRAS, 519, 1452, doi: [10.1093/mnras/stac3643](https://doi.org/10.1093/mnras/stac3643)
- Westfall, K. B., Cappellari, M., Bershad, M. A., et al. 2019, AJ, 158, 231, doi: [10.3847/1538-3881/ab44a2](https://doi.org/10.3847/1538-3881/ab44a2)
- Xu, C. K., Domingue, D., Cheng, Y.-W., et al. 2010, ApJ, 713, 330, doi: [10.1088/0004-637X/713/1/330](https://doi.org/10.1088/0004-637X/713/1/330)
- Xu, C. K., Cheng, C., Appleton, P. N., et al. 2022, Nature, 610, 461, doi: [10.1038/s41586-022-05206-x](https://doi.org/10.1038/s41586-022-05206-x)
- Yu, N., Ho, L. C., Wang, J., & Li, H. 2022a, ApJS, 261, 21, doi: [10.3847/1538-4365/ac626b](https://doi.org/10.3847/1538-4365/ac626b)
- Yu, Q., Fang, T., Feng, S., et al. 2022b, ApJ, 934, 114, doi: [10.3847/1538-4357/ac78e6](https://doi.org/10.3847/1538-4357/ac78e6)
- Zuo, P., Ho, L. C., Wang, J., Yu, N., & Shangguan, J. 2022, ApJ, 929, 15, doi: [10.3847/1538-4357/ac561f](https://doi.org/10.3847/1538-4357/ac561f)
- Zuo, P., Xu, C. K., Yun, M. S., et al. 2018, ApJS, 237, 2, doi: [10.3847/1538-4365/aabd30](https://doi.org/10.3847/1538-4365/aabd30)
- Zwaan, M. A., Meyer, M. J., & Staveley-Smith, L. 2010, MNRAS, 403, 1969, doi: [10.1111/j.1365-2966.2009.16188.x](https://doi.org/10.1111/j.1365-2966.2009.16188.x)